

A MeerKAT view of the Neutral Atomic Gas in Stephan's Quintet

K. RAJPUROHIT,^{1,*} E. O'SULLIVAN,^{1,*} G. SCHELLENBERGER,¹ J. M. VR TILEK,¹ L. P. DAVID,¹ S. GIACINTUCCI,² P. N. APPLETON,³
C. K. XU,^{4,5} C. CHENG,^{4,5,6} AND T. DEB¹

¹Center for Astrophysics | Harvard & Smithsonian, 60 Garden Street, Cambridge, MA 02138, USA

²Naval Research Laboratory, 4555 Overlook Avenue Southwest, Code 7213, Washington, DC 20375, USA

³Caltech/IPAC, MC 314-6, 1200 E. California Blvd., Pasadena, CA 91125, USA

⁴Chinese Academy of Sciences South America Center for astronomy, National Astronomical Observatories, CAS, Beijing 100101, People's Republic of China

⁵National astronomical Observatories, Chinese Academy of Sciences, 20A Datun Road, Chaoyang District, Beijing 100101, People's Republic of China

⁶CAS Key Laboratory of Optical Astronomy, National Astronomical Observatories, Chinese Academy of Sciences, Beijing 100101, People's Republic of China

ABSTRACT

We present new MeerKAT 21cm spectral line observations of the neutral hydrogen gas in the compact galaxy group Stephan's Quintet (HCG 92). These data provide a significantly improved view of the atomic gas distribution and kinematics in the group. New features include the first detections of HI associated with member galaxies NGC 7319 and NGC 7320C, the identification of an additional high-velocity HI component associated with SQ-A, and the detection of additional HI at low velocities filling much of the area of the NGC 7318B disk. We also find HI in the previously detected gas bridge linking NGC 7319 and NGC 7318B, and a new northern bridge linking NGC 7319 to the SQ-A star-formation region. We detect HI with a wide range of velocities along the line of sight through the northern half of the famous shock ridge, including in the 6200-6500 km s⁻¹ velocity range occupied by shocked H α emission. We examine the morphology and velocity structure of the HI and consider the origins of different components, finding some evidence that while the gas associated with NGC 7318B has been disturbed by its collision with the group, it may still retain a component of disk rotation. We find no gaseous connection between the tidal tails and NGC 7320C, but reaffirm the close connection between the shocked gas in the ridge (traced by X-ray, radio continuum and warm H₂ emission) and the southern tidal tail. Based on the integrated spectrum, we find a total HI mass in the group of $3.5 \pm 0.4 \times 10^{10} M_{\odot}$, higher than the VLA estimate and comparable to FAST.

Keywords: Galaxy collisions (585); Galaxy interactions (600); Galaxy groups (597); Hickson compact group (729); HI line emission (690); Intergalactic medium (813); Intergalactic filaments (811); Shocks (2086)

1. INTRODUCTION

Stephan's Quintet, also known as HCG 92 (Hickson 1982) is perhaps the most famous compact group of galaxies, and is certainly among the most extensively studied galaxy systems on any scale. Originally identified as an optical grouping of five galaxies (Stephan 1877), redshift measurements showed that one of the members (NGC 7320) is an unrelated foreground spiral galaxy. Of the remaining original members NGC 7317, NGC 7318A, and NGC 7319 form the core of the group (see Figure 1) with recession velocities in the range $\sim 6600\text{-}6750$ km s⁻¹ (Williams et al. 2002). The last major

galaxy, the highly inclined spiral NGC 7318B, appears to be falling through the group with a (blueshifted) relative velocity of ~ 900 km s⁻¹.

The group shows many signatures of a complex interaction history, including tidal tails, arms, and optical filaments in and around the NGC 7318A/B pair and NGC 7319, see Figure 1. Deep optical imaging shows an extensive filamentary halo of stellar emission surrounding and linking the galaxies (e.g., Duc et al. 2018; Duarte Puertas et al. 2019). However, the most spectacular feature of the group is a ~ 50 kpc S-shaped ridge of shocked gas running along the east side of NGC 7318B. This was originally discovered from its radio emission (Allen & Hartsuiker 1972; van der Hulst & Rots 1981, indicating the presence of relativistic electrons and a magnetic field) but also contains ~ 0.6 keV thermal plasma visible in the X-ray (Trinchieri et al. 2003, 2005; O'Sullivan

Corresponding author: Kamlesh Rajpurohit, Ewan O'Sullivan
kamlesh.rajpurohit@cfa.harvard.edu, eosullivan@cfa.harvard.edu

* These authors contributed equally to this work

et al. 2009), ionized gas traceable via $H\alpha$ emission (e.g., Arnaudova et al. 2024), molecular gas emitting via CO (e.g., Emonts et al. 2025; Maeda et al. 2025; Xu et al. 2025), H_2 (Appleton et al. 2023) and other lines (Appleton et al. 2013), as well as dust and star formation regions (e.g., Xu et al. 2003). The shock appears to have been driven by the collision of the intruder galaxy NGC 7318B with a pre-existing tidal filament of stripped gas (Sulentic et al. 2001), with the collision vector close to the line of sight.

Evidence for this earlier tidal structure has come primarily from HI line observations. Neutral hydrogen at the velocity of the group was first identified by Balkowski et al. (1973) and Shostak (1974), and the early interferometric (Allen & Sullivan 1980; Shostak et al. 1984) revealed gas components at roughly 5700, 6000 and 6600 km s^{-1} , including a curved tail extending several arcminutes east and north from the group, but little gas in the galaxies themselves. However, the detailed structure of the HI in the group was only fully established around the turn of the millennium, using Very Large Array (VLA) observations in C and D configurations (Williams et al. (2002); see also Verdes-Montenegro et al. (2001a)). These revealed four main structures: the previously identified HI arc extending east and north of the group, overlapping the optical tidal tails but following a more tightly curved path; a low-velocity component in the southwest, apparently associated with the disk of the intruder galaxy NGC 7318B; and two north-western components, both located on a line of sight centered on the crossed northeast/northwest arms in the north of NGC 7318A/B, but with recession velocities ~ 6000 and ~ 6600 km s^{-1} . The highest column densities in the northwest components and in the arc were found to be associated with regions of star formation. One (SQ-A) is a collision triggered starburst (Xu et al. 1999, 2025) the other (SQ-B) a tidal dwarf galaxy candidate (Xu et al. 1999; Lisenfeld et al. 2004). The radio continuum emission from the shock ridge was shown to fill the gap between the base of the HI arc and the northwest high-velocity component, suggesting the two had once formed an unbroken filament, with the HI in the ridge section since destroyed by the collision of NGC 7318B.

Later works have mainly focused on deep single-dish measurements in and around the group, seeking to measure the total mass of HI and identify any larger-scale structures. Additional diffuse HI not resolved by the VLA data is certainly present, with Green Bank Telescope (GBT) observations (Borthakur et al. 2010, 2015) finding masses at least double that reported from the VLA, and Five-hundred-meter Aperture Spherical Telescope (FAST) mapping producing a total HI mass estimate of $3.45 \times 10^{10} M_{\odot}$ (for an assumed distance of 85 Mpc, Xu et al. 2022; Cheng et al. 2023). These observations also reveal HI emission at 6200-6300 km s^{-1} and 6800-7000 km s^{-1} which was not reported from the VLA

Table 1. MeerKAT HI observations detail

Coordinates	RA: 22h35m57.5s Dec: +33d57'36.0"
Observation dates	19 December 2024 28 December 2024
Flux/bandpass calibrator	J0408-6545
Phase/gain calibrator	J2236+2828
Total integration time	6 h (2×3 h)
Correlator mode	32k, dual polarisation
Frequency range	0.9–1.7 GHz
Total bandwidth	856 MHz
Number of channels	32768
Channel Width	26.123 kHz
Spectral resolution	5.5 km s^{-1}

data. Both the single dish and older interferometer datasets detected HI in other nearby galaxies not originally classified as part of the group, but whose velocities suggest they may be part of a halo of smaller satellites.

While more recent analyses of the archival VLA data have shown more extended HI structure in the group, with hints of gas overlapping NGC 7319 (Jones et al. 2023), it remains the case that the interferometric HI data for Stephan’s Quintet is now more than 20 years old. We have observed the group using MeerKAT, with the goal of providing an updated view of its HI content and radio continuum emission. MeerKAT’s 64 dishes provide a well-sampled $u - v$ plane with exceptional sensitivity to the L-band continuum, and HI line sensitivity and a maximum resolvable scale similar to that of the VLA ($\sim 10'$). In , hereafter paper II we will present an analysis of the multi-frequency radio continuum data for the group, including the MeerKAT L-band continuum maps. In this paper, we present the results of our HI analysis of the group.

The layout of this paper is as follows: in Section 2, we present an overview of the observations and data reduction. The new HI images, overview of the detected structures, and integrated profiles and mass estimates are presented in Section 3. We end with a discussion and summary in Sections 4 and 5.

Throughout the paper, we assume a distance to Stephan’s Quintet (hereafter SQ) of 94 Mpc, for easy comparison with recent studies of the group (Appleton et al. 2023; Emonts et al. 2025; Aromal et al. 2025; Xu et al. 2025), and use the optical velocity definition. At this distance $1''$ corresponds to 456 pc. All output radio images are in the J2000 coordinate system and are corrected for primary beam attenuation.

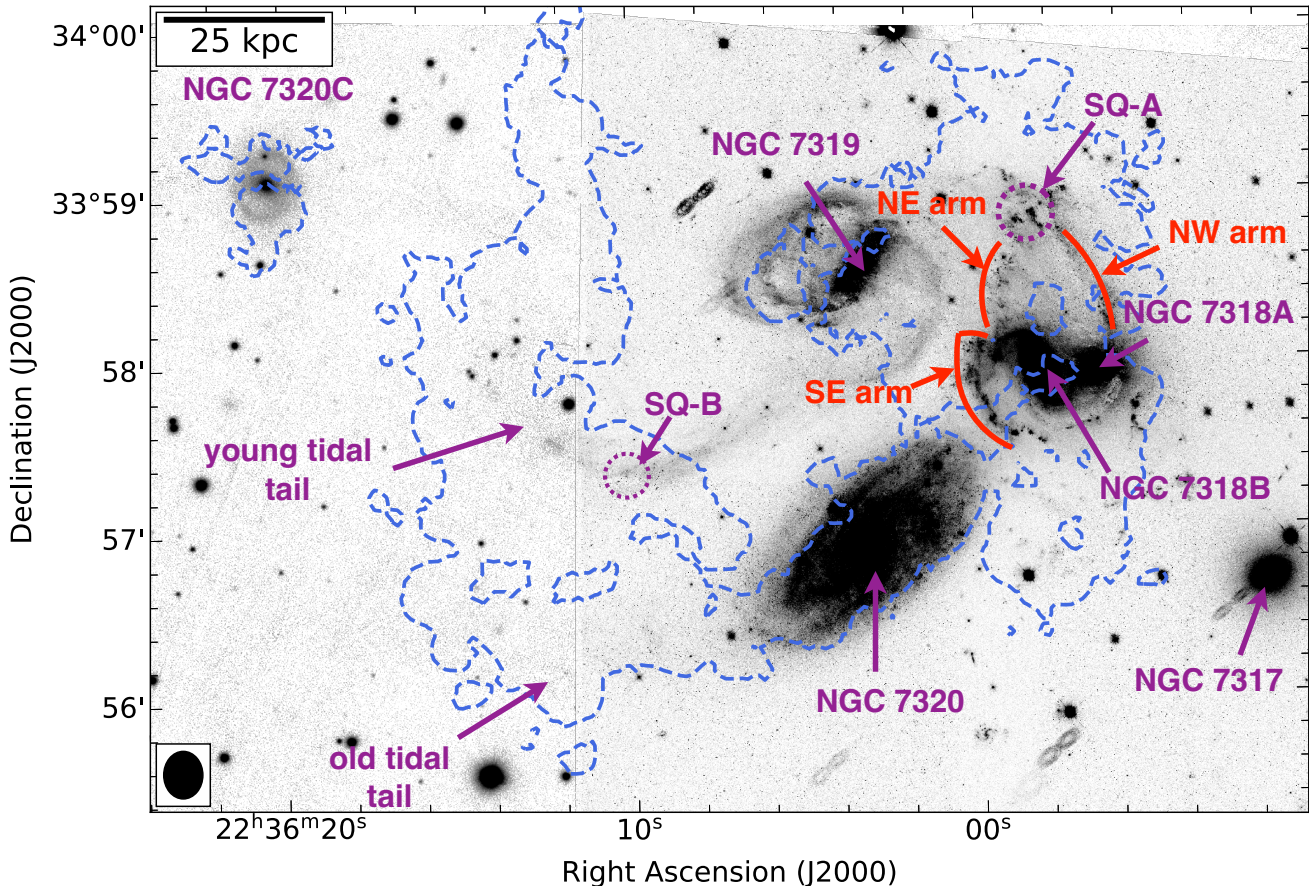


Figure 1. Outline map of the galaxies, stellar tidal features and HI distribution in Stephan’s Quintet. The combined *Hubble Space Telescope* (HST) and Digitized Sky Survey (DSS) optical image is overlaid with a MeerKAT HI contour drawn at $0.012 \text{ Jy beam}^{-1} \text{ km s}^{-1}$, corresponding to an HI column density of $5.6 \times 10^{19} \text{ atoms cm}^{-2}$. Spiral arms and arm-like features in NGC 7318B are labeled in red. The $17'' \times 14''$ synthesized beam size is indicated in the bottom left corner.

2. OBSERVATION AND DATA REDUCTION

The group was observed with MeerKAT using the L-band receiver and the 32k correlator mode, with an integration time of 8s. For observational details, we refer to Table 1. The MeerKAT observations were centered at 1283 MHz and had a channel width of 26.123 kHz, corresponding to a velocity resolution of 5.5 km/s. The large field of view of MeerKAT (HPBW $\sim 1^\circ$) enabled us to observe the group and its surroundings using a single pointing. However, due to its high declination, the source was observed in two separate observing runs (3×2 hrs on source time). For each run, scans of the primary calibrator (J0408-6545) for flux/bandpass calibration were made at the start and end of the observations (10 minutes each). The secondary calibrator (J2236+2828) scans were conducted every 30 minutes for 2 minutes. Additionally, J0108+0134 was observed as a polarization calibrator.

Each Meerkat observing run was processed using the Containerized Automated Radio Astronomy Calibration pipeline

(CARACal; Józsa et al. 2020)⁷. We proceed only with data covering the frequency range 1200-1520 MHz to limit the computing resources required for calibration and imaging. The data were calibrated on Hydra (the Smithsonian Institution High Performance Computing Cluster). To produce the final HI cube, the data were calibrated in three steps: cross-calibration, continuum imaging, and line imaging.

2.1. Cross Calibration

The first step in CARACal involved flagging shadowed antennas, autocorrelations, and known radio frequency interference (RFI) channels. Subsequently, AOflagger (Offringa et al. 2010) was employed to identify and remove additional low amplitude RFI-contaminated data. The frequency range covering Galactic emission was also flagged.

The primary calibrator J0408-6545 was modeled using the MeerKAT Local Sky Models within CARACal. Following this, cross-calibration was conducted to solve for time-

⁷ <https://ascl.net/2006.014>

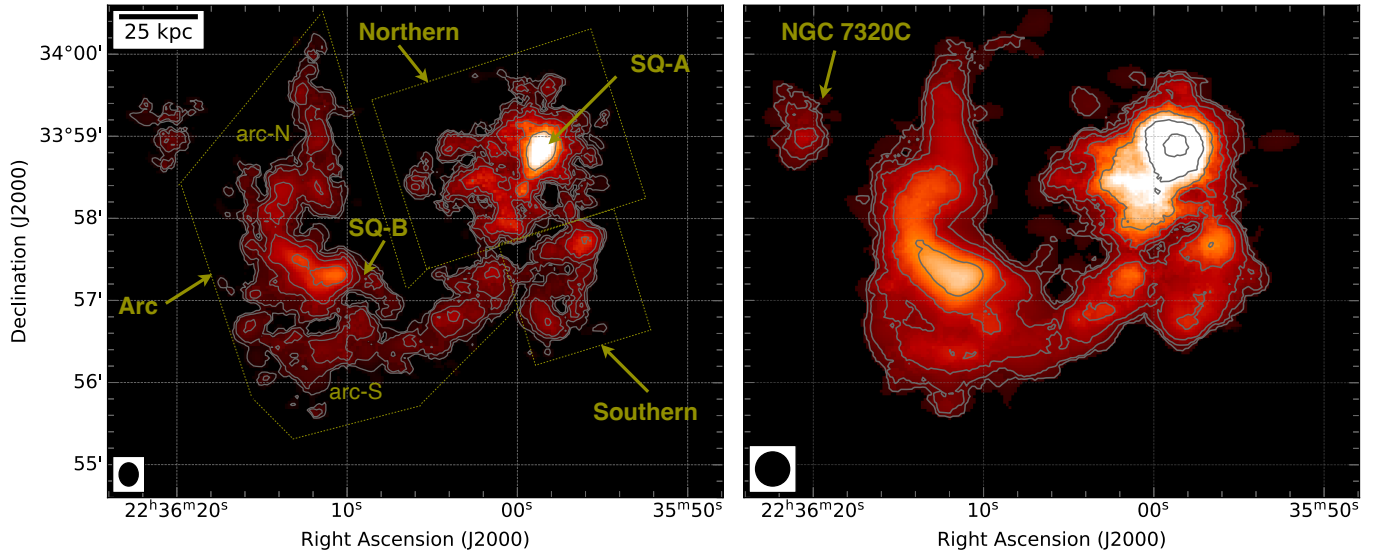


Figure 2. MeerKAT moment-zero maps at medium and low resolutions showing the total HI column density distribution in SQ. *Left:* the beam size is $17'' \times 14''$ and the contours are drawn at $5.6, 11.1, 22.3, 44.5, 89.1, 178 \times 10^{19}$ atoms cm^{-2} . *Right:* The beam size is $25'' \times 25''$ and the contours are drawn at $3.9, 7.8, 15.6, 31.1, 62.2, 124 \times 10^{19}$ atoms cm^{-2} . The MeerKAT observations reveal previously undetected HI emission in the group core, NGC 7319 and NGC 7320C.

Table 2. MeerKAT HI Cube Properties

Frequency range	1370–1425 MHz
Velocity range	−966.5 to 11030.1 km s^{-1}
Beam (high resolution)	$17'' \times 5.5''$, $d\nu = 5.5 \text{ km s}^{-1}$ rms = 0.20 mJy beam $^{-1}$
Beam (medium resolution)	$17'' \times 14''$, $d\nu = 16.5 \text{ km s}^{-1}$ rms = 0.18 mJy beam $^{-1}$
Beam (low resolution)	$25'' \times 25''$, $d\nu = 16.5 \text{ km s}^{-1}$ rms = 0.24 mJy beam $^{-1}$

Notes: The high and medium resolution HI cubes are created with Briggs weighting with `robust` = -0.5 while the low resolution one with `robust` = 0.0 without any taper. All reported rms values represent per-channel noise levels. $d\nu$ is the velocity resolution.

dependent delays and gain calibration. We then applied the Bandpass correction, applied the primary calibrator delay and bandpass solutions to the secondary calibrator and solved for time-dependent amplitude and phase corrections. All cross-calibration solutions were applied to the target field, after which the target field was also flagged for RFI using the same AOflagger strategy.

2.2. Continuum Imaging

After initial calibration, we created an initial image of the target field with WSClean (Offringa et al. 2014) within CARACal using multi-frequency (MFS) synthesis. The continuum imaging was performed using the Briggs weighting

scheme (Briggs 1995) with a robust parameter of -0.5 and uv taper of $10''$. These parameters were chosen to achieve an optimal balance between angular resolution and sensitivity, with the uv taper specifically applied to recover extended continuum emission.

For self-calibration, we employed CubiCal (Kenyon et al. 2018). After initial imaging, three rounds of phase-only self-calibration were performed, followed by a final round of amplitude-phase calibration. During each self-calibration step, the SoFia (Serra et al. 2015) source finder, integrated into CARACal, was used to produce a sky mask from the output deconvolved images. The self-calibration solutions were interpolated in frequency and transferred to the cross-calibrated target measurement set.

2.3. Line imaging

We subtracted the continuum model created in the previous step from the calibrated visibilities (both observing runs) using the task `mstransform` in CARACal. Additionally, Doppler-tracking corrections and a fourth-order polynomial fitting to the visibilities are used to remove any residual continuum emission. After this the HI data cube was produced with WSClean, with a Briggs weighting with `robust` value $r = -0.5$, multiscale cleaning, and without any uv-taper. This resulted in an angular resolution of $17'' \times 5.5''$. As noted above, the maximum resolvable angular scale with the MeerKAT is $\sim 10'$.

Throughout this paper, we use two HI data cubes, referred to as the medium and low resolution cubes. Both cubes were smoothed in velocity, resulting in spectral-line maps with a velocity resolution of 16.5 km s^{-1} (3-channel smoothing).

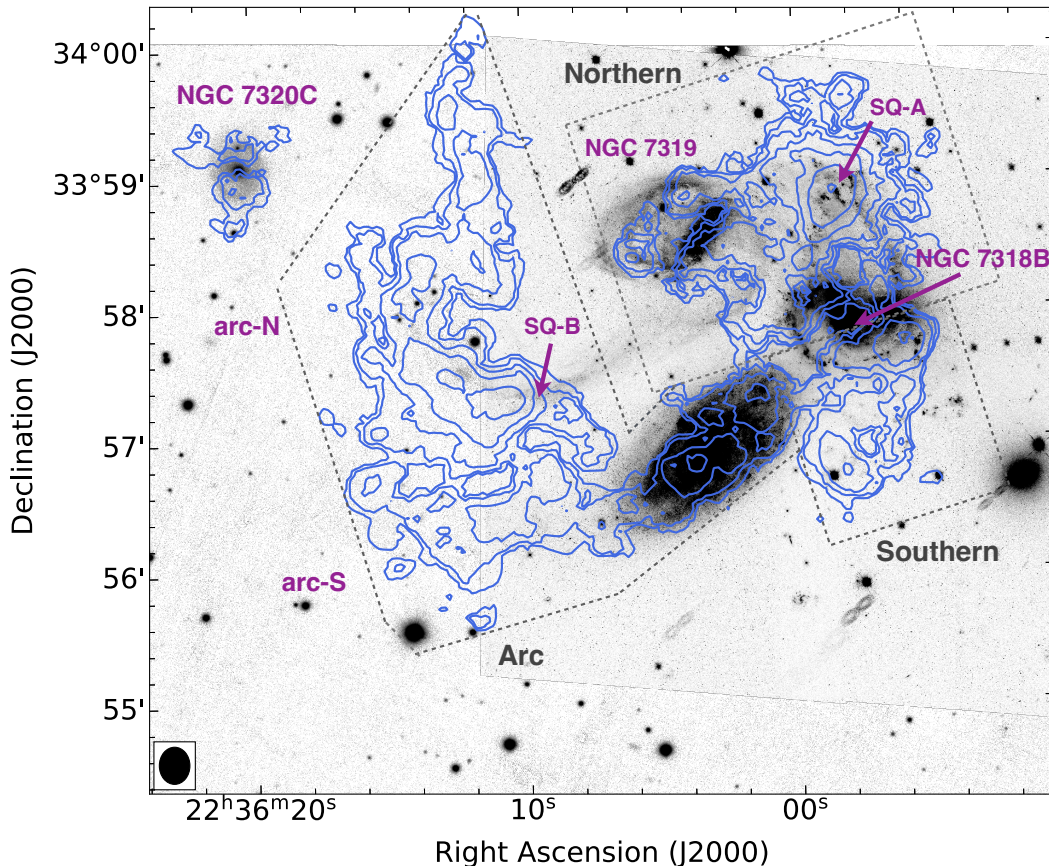


Figure 3. *Top:* HST+DSS image overlaid with HI column density and radio continuum contours. The HI image beam size is $17'' \times 14''$ and the contours are drawn at 5.6, 11.1, 22.3, 44.5, 89.1, 178×10^{19} atoms cm^{-2} (left panel).

The medium-resolution HI cube has a synthesized beam of ($17'' \times 14''$), obtained by smoothing the highest-resolution cube (i.e., $17'' \times 5.5''$). This allowed us to make a direct comparison with the previously published VLA HI cube reported in Williams et al. (2002). The single channel median rms noise in this cube is $180 \mu\text{Jy beam}^{-1}$. The 3-sigma HI flux limit is about 0.009 Jy km/s , corresponding to an HI column density limit of 4×10^{19} atoms cm^{-2} . The low-resolution cube has a beam size of $25''$, created with Briggs robust weighting (robust = 0.0). The properties of the HI cubes are summarized in Table 2. We also examined the MeerKAT data for evidence of OH line emission from the group, but none was found.

3. RESULTS: HI PROPERTIES IN STEPHAN'S QUINTET

Figure 2 shows our new MeerKAT total intensity HI emission in the direction of SQ at the two spatial resolutions described above: $17'' \times 14''$ and $25'' \times 25''$. The excellent sensitivity of MeerKAT allowed us to probe the HI emission with exceptional detail. The HI emission is mainly distributed in three distinct spatial regions: the Arc, Northern (northwest high-velocity, northwest low-velocity in Williams

et al. 2002) and Southern (southwest in Williams et al. 2002). Within the northern region, the strongest HI flux is seen from a relatively compact region roughly centered on the starburst region SQ-A. We recovered the HI associated with all previously identified features and robustly detected additional, previously unseen emission. The morphology and properties of the individual features are discussed in the following section.

3.1. Overview of HI structure

The most extended and diffuse HI emission is associated with the "Arc", a prominent L-shaped feature extending over $5.3'$ (about 140 kpc) east and southeast of the group (Figure 2). In the MeerKAT maps, its morphology is consistent with that reported previously by Williams et al. (2002) and Jones et al. (2023) from the VLA observations.

Figure 3 shows the HI distribution overlaid on an optical image (combined *Hubble* and Digitized Sky Survey) of the group. The arc structure overlaps the two optical tidal tails, the northern young tail extending southeast from NGC 7319, which includes the star-formation region SQ-B, and the southern old tail extending southeast from behind NGC 7320. The arc has a distinct gap between the lower HI

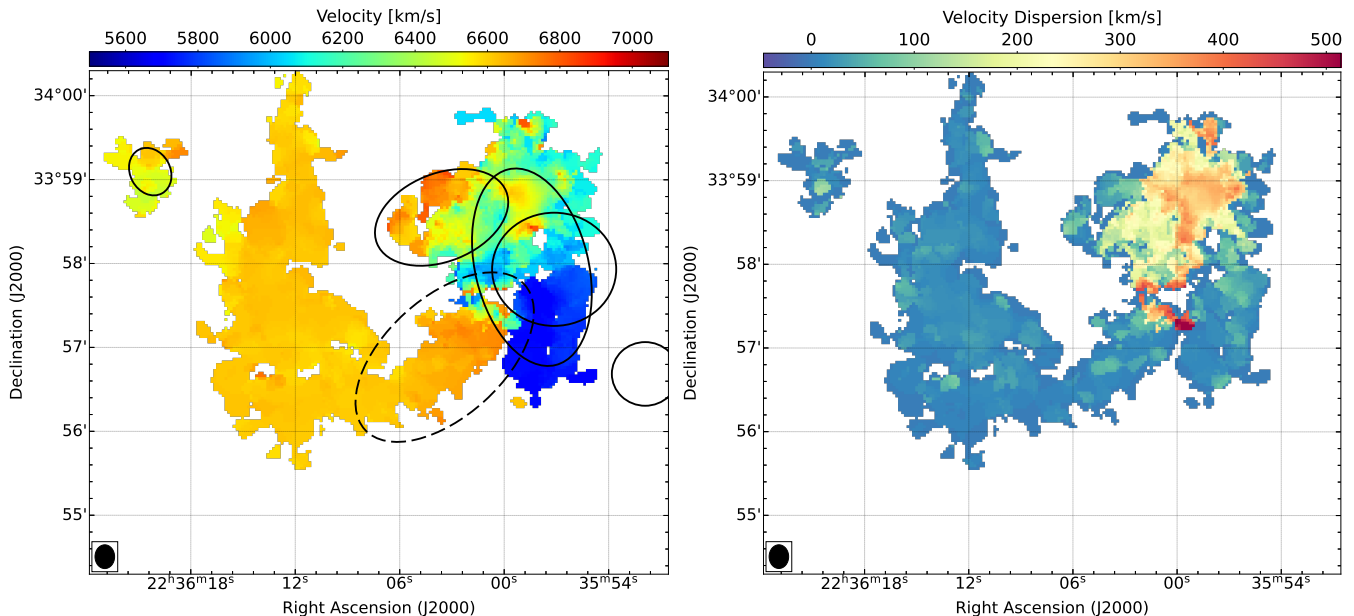


Figure 4. HI moment-one (Left) and moment-two (Right) maps of Stephan’s Quintet obtained from SOFIA. The solid black outlines mark the D_{25} ellipses of the group member galaxies, using parameters from the LEDA catalogue, while the dashed ellipse marks the foreground galaxy. These maps have a beam size of $17'' \times 14''$. Beam sizes are indicated in the bottom-left corner of each image.

column-density gas in the southern tail (arc-S) and the higher column densities around SQ-B (arc-N), see Figures 2 and 3. Arc-N and arc-S appear to align with the optical tidal tails. Williams et al. (2002) posited such a separation, but the gap between the two components is considerably clearer in the MeerKAT data than it was in the VLA.

The arc has a mean radial velocity of about 6624 km s^{-1} and a very low velocity dispersion of about 10 km s^{-1} (see Figure 4). The radial velocity is comparable to that found with the VLA (6610 km s^{-1}). Unlike Williams et al. (2002), we do not find any evidence for differences in kinematics or velocity dispersion between arc-N and arc-S. However, as in the VLA data, MeerKAT shows a velocity gradient at the base of arc-S, where it passes behind the foreground spiral galaxy NGC 7320 ($v_{rec}=775 \text{ km s}^{-1}$, Springob et al. 2005), with velocity increasing toward the northwest (Figure 4). Interestingly, in the L-band MeerKAT continuum image (Paper I), we find radio emission located along the northern optical tail but also between the two optical tails i.e., in the region separating arc-N and arc-S.

Within the arc, we identify two high column density clumps in the vicinity of SQ-B, though neither coincides with its position. The $25''$ -resolution maps (Figure 2 right panel) show an additional spur of HI extending northwest along the base of the northern optical tail almost to NGC 7319, adding to the evidence that there are indeed two separate HI tails. To the east of the Arc lies the spiral galaxy NGC 7320C, which we detect in HI for the first time (see Figure 2). We find no evidence of HI connecting arc-N and NGC 7320 but note that the gas velocities of the two are very similar (Figure 3).

A large fraction of the HI emission in the MeerKAT observation is detected in the bright northern region. Previous studies found this to consist of two components, both centered in the northern part of NGC 7318A/B around the starburst region SQ-A, but separated in velocity (Williams et al. 2002; Shostak et al. 1984). Our new observations reveal additional HI emission in this region, including the first clear detection of HI associated with NGC 7319. The northern components cover $\sim 2.5'$ east-west (corresponding to a physical size of $\sim 70 \text{ kpc}$) and extend significantly further south than was seen with the VLA, through much of the northern half of NGC 7318A/B and particularly along the eastern arms of NGC 7318B (see Figures 2 and 4). The peak HI emission is detected around the star-forming region SQ-A. By contrast, the nuclei of NGC 7318A and B show little to no HI emission, and the region immediately to their north, between the shock ridge and northwestern spiral arm is HI-free. As evident from the moment-one and two maps (Figure 4), the entire northern region spans a wide velocity range ($6000\text{--}7000 \text{ km s}^{-1}$) and exhibits a high velocity dispersion (about 400 km s^{-1}).

We detect HI emission extending across much of the disk of NGC 7319 (Figure 3). The HI in the disk has an average radial velocity of 6686 km s^{-1} , similar to but somewhat below the systemic velocity of $6740 \pm 50 \text{ km s}^{-1}$ derived from stellar absorption line measurements (Aoki et al. 1996). Nonetheless, this represents the first confirmed detection of HI in NGC 7319. The spatial distribution of the HI is broadly similar to the CO(2-1) molecular gas distribution found by (Emonts et al. 2025, see Figure A.3). CO emission

peaks in the core of NGC 7319 (Seyfert-2 AGN) but while HI is present, no equivalent peak is found, indicating that the molecular-to-atomic mass ratio differs from core to disk, or that excitations conditions vary.

The remaining HI emission in the direction of SQ is found in a diffuse low velocity cloud located south of the cores of NGC 7318A/B, labeled as Southern region in Figure 3. The morphology and extent of this feature are similar to that reported from the VLA data. It has a mean radial velocity of 5754 km s^{-1} , the lowest of any of the HI components, and a velocity dispersion of about 28 km s^{-1} (see Figure 4). It covers the southwestern part of the NGC 7318B SE spiral arm and extends considerably further south, overlapping a number of weaker stellar structures sometimes referred to as the "southern debris region" which may be part of the NGC 7318B disk. Notably, while the southern component abuts the northern component on the west side of NGC 7318A, in the east there is a distinct gap between the two.

3.2. Integrated HI Profiles

We extracted integrated HI line profiles for the four main regions described above (arc, southern region, northern region, and SQ-A). We used the medium-resolution MeerKAT HI cube ($17'' \times 14''$ beam size) to extract the spectra. The resulting integrated profiles are shown in Figure 5. The regions from which the profiles were extracted are shown in Figure A.1. We note that SQ-A is a subset of the northern region, and the spectra of the latter include all flux density from the former. Past studies have shown considerable velocity structure around SQ-A (Xu et al. 2025), and we thus consider it worthwhile to examine it separately as well as in combination with the larger-scale northern emission.

The overall HI profile shape for the combined spectrum of SQ is similar to those found with the VLA and FAST (see Figure A.2; Williams et al. 2002; Cheng et al. 2023). The HI emission is detected over the velocity range 5500 to 7100 km s^{-1} . As with several previous studies (e.g., Duarte Puertas et al. 2019; Maeda et al. 2025), we divide the spectrum into five velocity subcomponents, chosen based on the velocity structures in the integrated profiles: 5700 component ($5650\text{-}5950 \text{ km s}^{-1}$), 6000 component ($5950\text{-}6200 \text{ km s}^{-1}$), 6300 component ($6200\text{-}6500 \text{ km s}^{-1}$), 6600 component ($6500\text{-}6800 \text{ km s}^{-1}$), 6900 component ($6800\text{-}7050 \text{ km s}^{-1}$). The strongest emission peak is seen at $\sim 6600 \text{ km s}^{-1}$, the second strongest at $\sim 6000 \text{ km s}^{-1}$, and we detect significant flux between these two as well as at more extreme velocities (Figure 5).

The three distinct emission peaks associated with the 5700 , 6000 , and 6600 velocity components (see Figure 5 panel e) have peak flux densities of 11 mJy , 19 mJy , and 85 mJy respectively. These three components are reported in the

VLA and FAST observations (Williams et al. 2002; Jones et al. 2023; Cheng et al. 2023). An additional weaker peak at higher velocities (6900 component) and lower-level intermediate-velocity emission (6300 component) were only detected in the FAST observations (Cheng et al. 2023). The distribution of the relative flux densities in our new MeerKAT HI profile is different from that of the VLA. For example, the peak flux density reported by Williams et al. (2002); Jones et al. (2023) for the 6600 component is lower by a factor of 1.5 than that found by MeerKAT. This discrepancy indicates additional HI emission recovered with MeerKAT, thanks to its excellent sensitivity and dense inner $u - v$ coverage.

Compared to the single-dish FAST, GBT, and Arecibo data, MeerKAT recovers higher relative flux densities than GBT, values comparable to Arecibo, and lower values than FAST. Overall, the MeerKAT fluxes in the fainter 6300 and 6900 components are very similar to those found by FAST. However, the three main velocity components peaks (5700 , 6000 , 6600) detected with MeerKAT have peak flux densities lower than those from FAST (by a factor of $1.1\text{-}1.2$). This difference can be partly attributed to resolution, as the FAST spectrum is obtained from a $2.9'$ resolution map. It is worth mentioning that NGC 7320C was not resolved by FAST, so flux from this galaxy is included in the FAST spectrum but not in Figure 5. However, MeerKAT does resolve the galaxy, allowing us to treat it as a separate source.

The spectrum of the Arc structure shows a single narrow peak at $\sim 6600 \text{ km s}^{-1}$, as in all previous HI observations (Figure 5 panel c). Although it shows two distinct morphological features (arc-S and arc-N), the spectrum shows no evidence for multiple kinematic components. The southern region is similarly restricted to the low velocity 5700 component, again consistent with prior observations. However, unlike the Arc, in the southern region we find significant velocity substructure, with three velocity peaks (Figure 5, panel d).

The dominant northern region shows the broadest profile with three distinct velocity components: 6000 , 6600 , and 6900 (Figure 5 panel b). This is the first detection of the 6900 component in interferometric HI data, and we measure an average radial velocity for this component of 6920 km s^{-1} . While HI emission from this 6900 component was previously found in single-dish data (Cheng et al. 2023) it was associated with the group as a whole; MeerKAT now shows it to be primarily located in and around SQ-A (see Figure 5 panel a). This is consistent with molecular line observations (Emonts et al. 2025). The 6000 and 6600 components correspond to the NW-LV and NW-HV structures identified from the VLA data (Williams et al. 2002) but we observe significant flux between these two peaks (the 6300 component) which was not seen by the VLA. We also see emission down to low veloc-

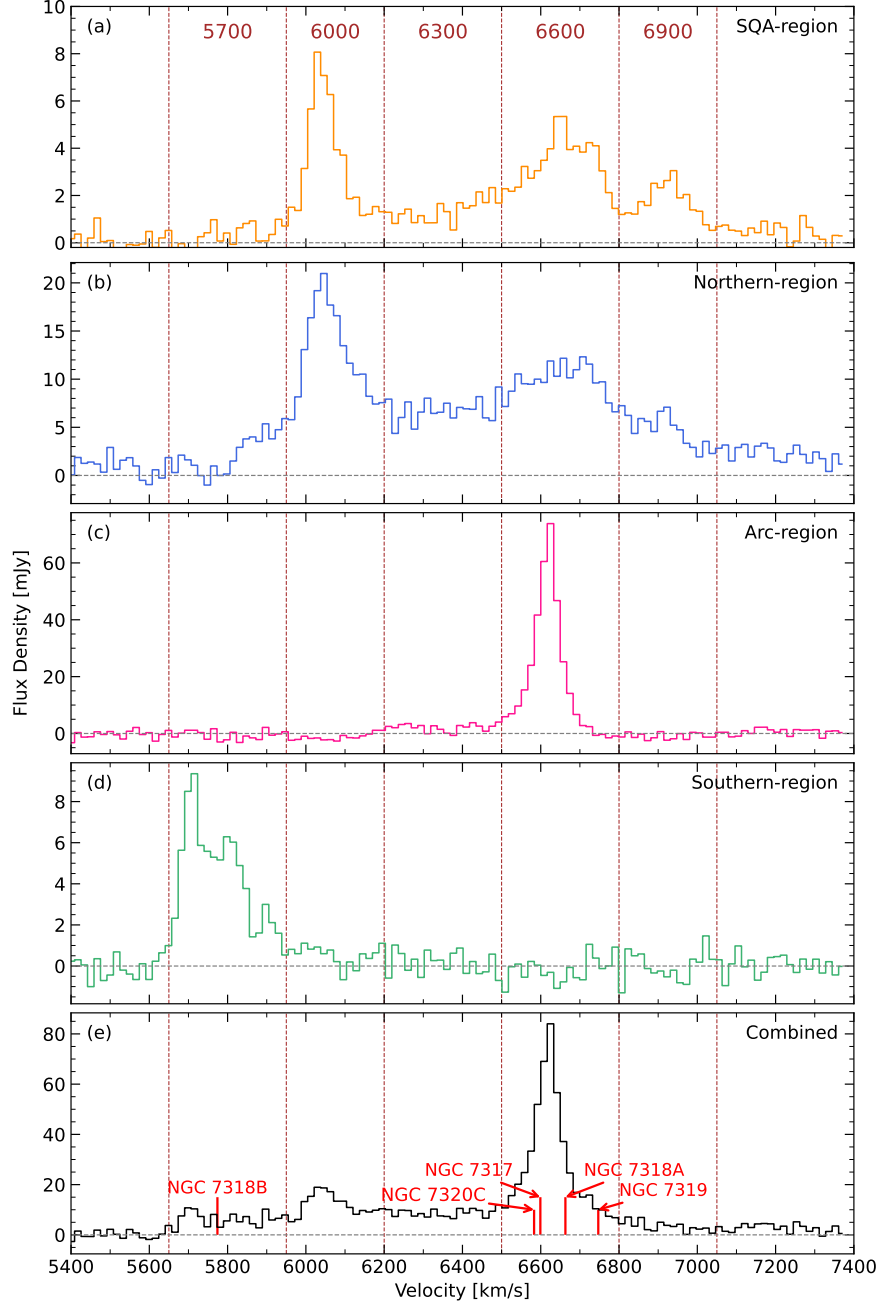


Figure 5. Spectra of the total HI emission and of individual subregions in SQ. The brown vertical dashed lines mark the boundaries of the five kinematical components, namely 5700, 6000, 6300, 6600, and 6900. The dashed gray horizontal lines indicate the zero flux density level and red lines (with labels) mark the optical velocities of the major group member galaxies. Figure A.1 shows the regions used to extract these. We note that the spectrum of the northern region includes the SQ-A region.

ities ($\sim 5800 \text{ km s}^{-1}$) in the northern region but notably not in SQ-A.

From the combined MeerKAT spectrum, we estimate the total integrated line flux density $S_{\text{int}} = \int S_{\nu} dv$ (in units of Jy km s^{-1}) by summing S_{ν} covering the detected HI emission between 5500 and 7100 km s^{-1} . The uncertainties in the flux density reported in this work include the rms and the flux scale errors which we assume to be 10%. From the spectrum,

we obtain a total HI flux density of $17.2 \pm 2.0 \text{ Jy km s}^{-1}$ for the group as a whole, which is 2.4 times higher than reported from the VLA (7 Jy km s^{-1} , Williams et al. 2002) and 1.4 times higher than the GBT measurement (12 Jy km s^{-1} , Jones et al. 2023). Our measured total integrated flux density is slightly lower than the FAST value of $20.5 \pm 2 \text{ Jy km s}^{-1}$ but consistent within the uncertainties (i.e., 1.2σ discrep-

Table 3. HI Kinematical components of Stephan’s Quintet

Region	Component	Velocity range (km s^{-1})	Integrated flux density (Jy km s^{-1})	M_{HI} (MeerKAT) ($\times 10^9 M_{\odot}$)	M_{HI} (VLA) ($\times 10^9 M_{\odot}$)	Figure
Total						
Integrated Spectrum	total	5400-7400	17.2 ± 2.0	35.0 ± 4.0		Figure 5
Spatially Resolved Maps	total	5400-7400	11.9 ± 1.2	24.0 ± 2.0	13.4 ± 1.6	Figure 3
Main Structures						
Arc	total	6200-6800	4.8 ± 0.5	9.8 ± 1.0	8.4 ± 0.9	Figure 3
	arc-N	6200-6800	3.2 ± 0.3	6.5 ± 0.6		
	arc-S	6200-6800	1.6 ± 0.2	3.3 ± 0.4		
Northern	total	5400-7400	6.0 ± 0.6	12.0 ± 1.0	3.7 ± 0.4	Figure 3
Southern	total	5400-7400	1.1 ± 0.1	2.4 ± 0.3	1.8 ± 0.2	
Substructures						
5700 & 6000 components	total	5650-6200	3.2 ± 0.3	6.6 ± 0.7		Figure 6
	5700	5650-5950	1.2 ± 0.2	2.5 ± 0.3		
	6000	5950-6200	2.0 ± 0.3	4.1 ± 0.5		
N7319		5400-7400	0.57 ± 0.06	1.2 ± 0.1		Figure 3
SQ-A	total	5400-7400	1.70 ± 0.10	3.5 ± 0.4		Figure 3
		6800-7050	0.20 ± 0.02	0.4 ± 0.04		Figure 7
		6500-6800	0.69 ± 0.07	1.4 ± 0.1		Figure 7
		5950-6200	0.62 ± 0.06	1.3 ± 0.1		Figure 6
SQ-B	total	5400-7400	0.25 ± 0.02	0.50 ± 0.04		
northern bridge	total	5400-7400	0.36 ± 0.04	0.73 ± 0.08		Figure 7
		6500-6800	0.24 ± 0.03	0.49 ± 0.06		
southern bridge	total	5400-7400	0.38 ± 0.04	0.78 ± 0.08		Figure 6
		6200-6500	0.10 ± 0.02	0.19 ± 0.02		

Notes: The total HI mass (i.e., Arc + Southern + Northern, excluding NGC 7320C) is obtained using two methods: (i) the flux density measured from the combined integrated spectrum, and (ii) the flux density measured from the `SoFIA`-generated pixel-wise maps at $25''$ resolution. The HI masses of the substructures are derived from the $17'' \times 14''$ resolution HI maps. VLA masses have been recalculated from the reported integrated fluxes using our adopted redshift and distance.

ancy). We note that the FAST total flux density includes an additional 0.2 Jy km s^{-1} contribution from NGC 7320C.

We also estimate the HI integrated flux density from `SoFIA` generated maps by applying 3-Dimensional masks on a channel by channel basis. The pixels outside the masks are set to zero. The advantage of this approach is that the channel-by-channel masks exclude pixels without HI emission and provide a higher signal-to-noise ratio. However, it may also exclude some pixels containing low-level emission, reducing the overall flux density measured for some regions. In Table 3, we summarize the MeerKAT HI global properties for SQ and subregions. This method resulted in a total HI integrated flux density of $11.9 \pm 1.2 \text{ Jy km s}^{-1}$, lower than that obtained from the HI spectrum but higher than reported by Williams et al. (2002) using the VLA. We emphasize that all integrated HI flux density measurements and HI mass estimates reported for sub-regions within SQ are, un-

less otherwise stated, obtained from maps (medium and low resolution) generated with `SoFIA`.

3.3. Velocity substructures

Figures 6 and 7 show moment-zero, one, and two maps for the five velocity ranges described above. These provide a more detailed view of the spatial distribution of the various velocity components and, in some cases, a clearer view of their kinematics. We also examined more finely-binned channel maps from the group, but given the wide velocity range of the HI emission and high spectral resolution of the MeerKAT data, we do not reproduce them here.

Figure 6 shows the low (5700, 6000) and intermediate (6300) velocity slices. The 5700 component shows two distinct clumps, the southern component discussed above and a smaller clump on the east side of NGC 7318B covering the shoulder of its southeastern spiral arm and extending to-

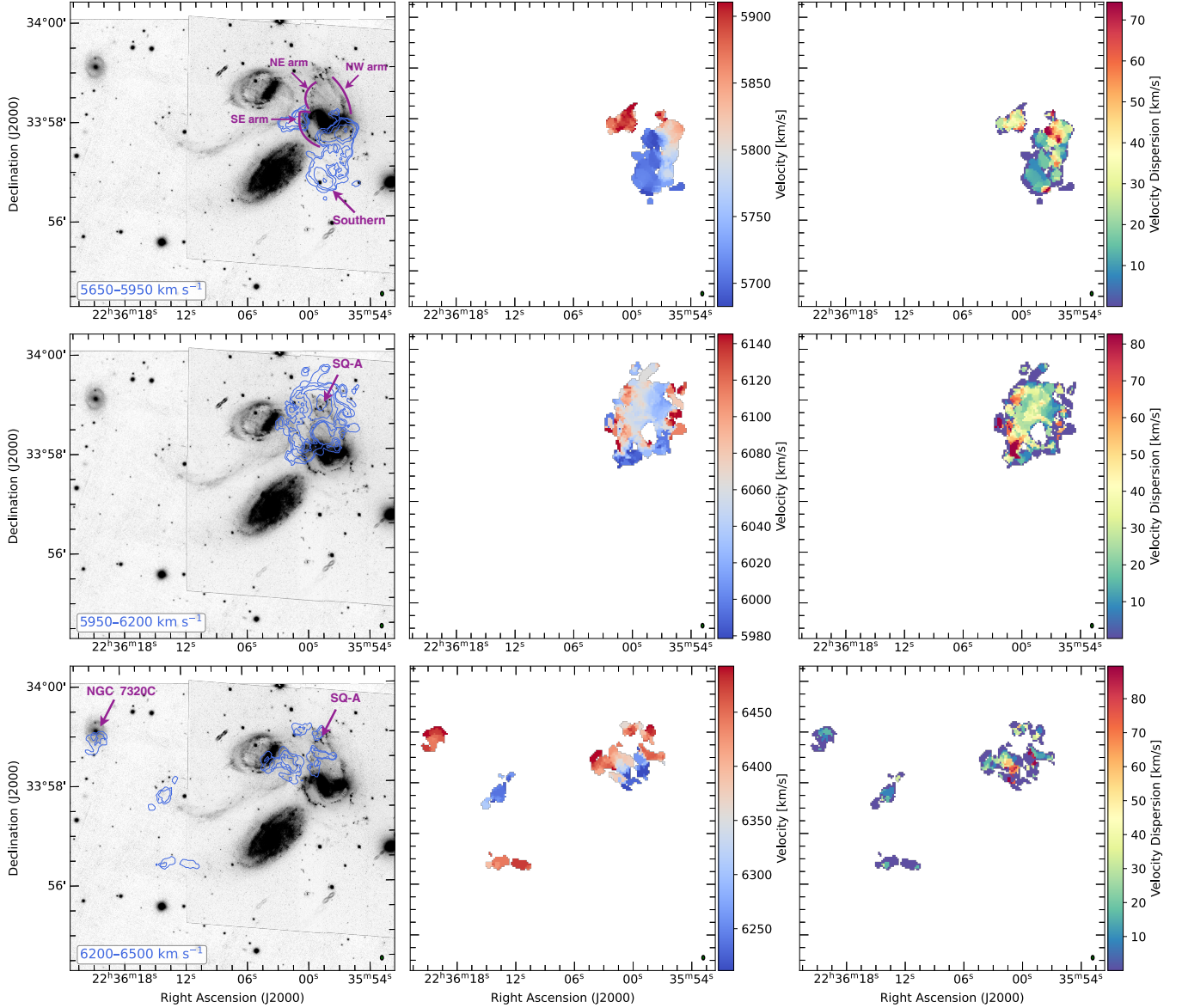


Figure 6. MeerKAT moment-zero (left), moment-one (middle) and moment-two (right) maps for the 5700, 6000 and 6300 km s^{-1} components. HI contour level are plotted at 5.6, 11.1, 22.3, 44.5, 89.1, 178..... $\times 10^{19}$ atoms cm^{-2} . The radio beam size is $17'' \times 14''$.

ward NGC 7319 (top-panel). The latter overlaps emission in the 6000 component, which extends north from this position along the northeast arm (and shock ridge), peaks around SQ-A, and continues down the west side of NGC 7318A/B along the northwest arm (Figure 6 middle-panel). As noted above, this northern low-velocity component is considerably more extended than the VLA data suggested. The moment-one maps of the two low velocity components show evidence of east-west velocity gradients in both components, with higher velocities seen on the west side of the southern (5700) component, and on the east side of the northern (6000) component.

The intermediate velocity emission (6300 component) is resolved into a number of smaller clumps or agglomera-

tions of HI (Figure 6 bottom-panel). These include gas in NGC 7320C, and small clumps in arc-S and arc-N coincident with the optical tidal tails but notably not associated with the star-formation regions of the northern (younger) tail. In the northern region, we see intermediate velocity gas near SQ-A, south of SQ-A in the northern part of the shock ridge, northeast of SQ-A, and extending west from the core of NGC 7319 across its disk toward the shock ridge. The moment one map suggests a gradient across this latter feature, which also overlaps lower-velocity gas at its eastern end (and higher-velocity gas in the west). This is the "bridge" structure reported across multiple wavebands, and whose velocity gradient was found from the ACA CO(2-1) data (Emonts et al. 2025).

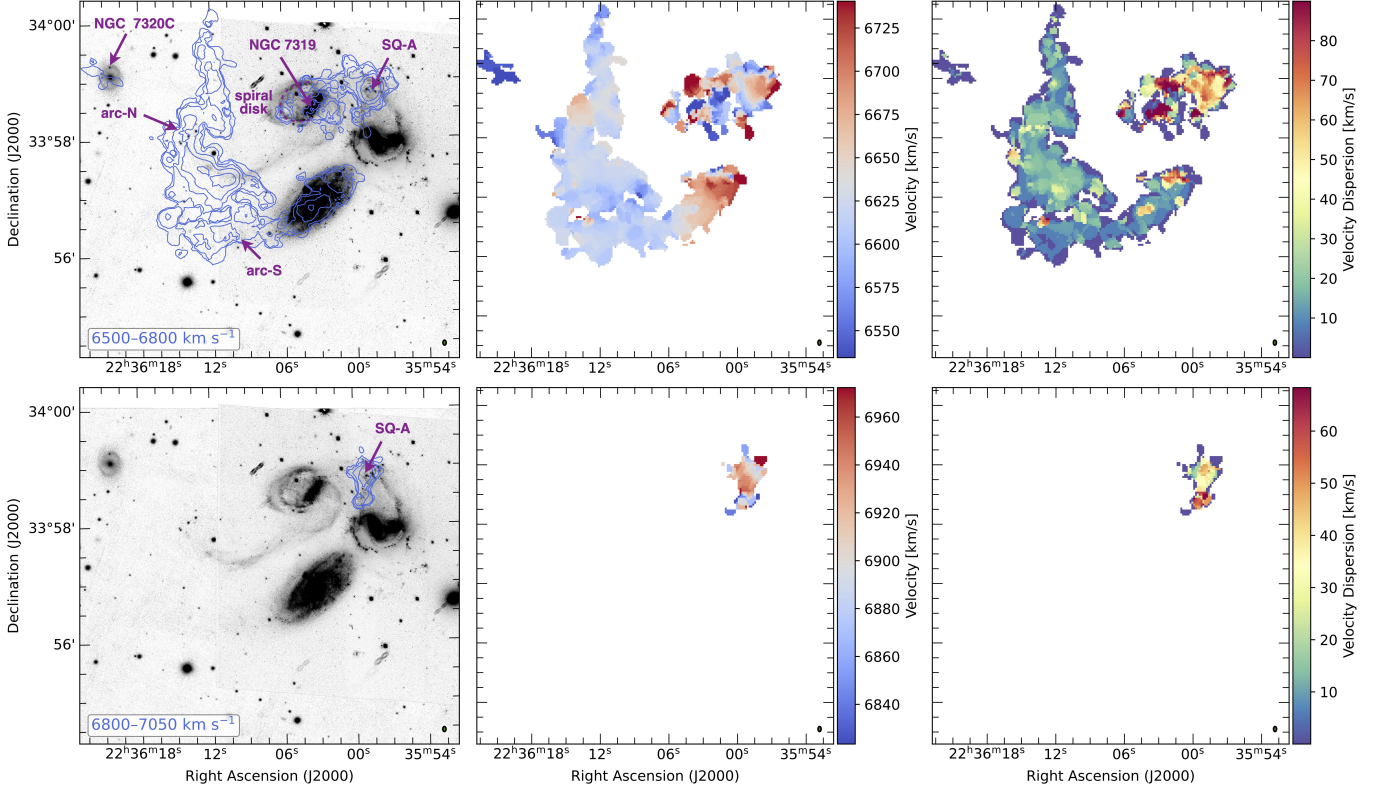


Figure 7. MeerKAT moment-zero (left), moment-one (middle) and moment-two (right) maps for the 6700 and 6900 km s^{-1} components. HI contour levels are plotted at $5.6, 11.1, 22.3, 44.5, 89.1, 178, \dots \times 10^{19}$ atoms cm^{-2} . The radio beam size is $17'' \times 14''$.

Figure 7 shows the high-velocity (6600, 6900) components. As expected, much of the 6600 emission is found in the arc structure, with a relatively flat velocity distribution except at the base of arc-S, where there is a gradient with increasing velocities to the north (top-panel). We also see additional HI associated with NGC 7320C. In the northern component, the emission peaks around SQ-A, with extensions southeast along the shock ridge, northwest, and particularly to the northeast, where we see a second, northern bridge, linking SQ-A to the northwest side of NGC 7319. The HI associated with NGC 7319 is mainly found in the western disk (at the base of the southern bridge) and in clumps in the northeast and southeastern parts of the galaxy, a similar distribution to that found for CO(2-1) emission with ACA. The velocity structure of the northern component is complex, but in the $25'' \times 25''$ maps we see hints of higher velocities in the northeast quadrant of NGC 7319, and lower velocities in its southwest quadrant, again in agreement with CO(2-1).

Finally, the highest velocity gas in the group (6900 component) is found in and around SQ-A, with an extension southeast along the shock ridge, and a stub extending east in the direction of the northern bridge linking across to NGC 7319 (Figure 7 bottom-panel). This is the most compact velocity component, but is still quite clearly aligned with the stellar structures in the shock ridge (the northeast arm).

3.4. HI mass estimates

We estimated the HI mass using the formula:

$$\frac{M_{\text{HI}}}{M_{\odot}} = \frac{2.36 \times 10^5 D_L^2}{(1+z)} \int S_{\nu} dv, \quad (1)$$

where D_L is the luminosity distance to the group in Mpc (i.e., 94 Mpc). For comparison with the HI mass estimate from the FAST observations, we follow Cheng et al. (2023) in using the integrated flux density from the MeerKAT combined spectrum (see Section 3.2). This yields a total mass estimate of $3.5 \pm 0.4 \times 10^{10} M_{\odot}$ for SQ, comparable to the FAST mass estimate of $4.2 \pm 0.5 \times 10^{10} M_{\odot}$. For a more direct comparison with the VLA mass estimate, we use the total (spatially filtered) integrated flux density measured from the SOFIA $25''$ map (see Table 3). This results in a lower HI mass estimate of $2.4 \pm 0.2 \times 10^{10} M_{\odot}$, but this is still a factor ~ 1.8 greater than that reported Williams et al. (2002) using the VLA, reflecting the additional flux captured by MeerKAT.

Following Williams et al. (2002), we estimate the mass in three main HI features in SQ, namely the Arc, Southern, and Northern regions (see Figure 2). The integrated flux densities and the corresponding HI masses of these regions are listed in Table 3. For the Southern region and Arc, we measured total HI masses of $2.4 \pm 0.3 \times 10^9 M_{\odot}$ and $9.8 \pm 1.0 \times 10^9 M_{\odot}$, respectively, slightly higher than found with the VLA. For the

Northern region, our mass estimate is $12.0 \pm 1.0 \times 10^{10} M_{\odot}$, which is significantly higher than reported by Williams et al. (2002) (see Table 3). This reflects the considerably larger spatial extent of the Northern region in the MeerKAT data, the addition of the new 6900 component, and previously unseen flux at low and intermediate velocities (5700 and 6300 components).

To measure the HI mass of the smaller distinct regions, we used the medium-resolution maps, which better resolve and separate these individual structures. The atomic mass estimates for the northern and southern bridges are challenging because these features are detected over multiple velocity components (see Section 4). Therefore, we measure their masses both over the full velocity range and over the more restricted ranges where the bridges are clearly detected. Using this conservative approach, we constrain the mass of the northern bridge to the range $4.9 \times 10^8 M_{\odot} < M_{\text{HI,Nbridge}} < 7.3 \times 10^8 M_{\odot}$ and the southern bridge to $1.9 \times 10^8 M_{\odot} < M_{\text{HI,Sbridge}} < 7.8 \times 10^8 M_{\odot}$. Emonts et al. (2025) reported a molecular gas mass for the southern bridge of $M_{\text{H}_2} = (2.3 \pm 0.5) \times 10^8 \alpha_{\text{CO}} M_{\odot}$, and noted that the CO conversion factor α_{CO} is unknown in SQ, with plausible values ranging from ~ 0.4 up to the canonical value for the Milky Way, $\alpha_{\text{CO}}=4.6$. Nonetheless, this molecular gas mass is comparable to our estimated HI mass within uncertainties. This suggests that the molecular and atomic gas components contribute similar amounts to the total gas mass in this region. Such a molecular-to-atomic gas ratio is probably a little higher than that found in the outer disks of nearby spirals (Leroy et al. 2008; Schruba et al. 2011) but as uncertainties are large and the southern bridge extends across the entire disk of NGC 7319, it is difficult to make a direct comparison.

For SQ-A, when considering the entire velocity range (for the used region see Figure A.1) we obtained a total mass of $3.5 \pm 0.4 \times 10^9 M_{\odot}$. The HI mass of the individual velocity subcomponents range from $0.4 - 1.4 \times 10^9 M_{\odot}$. The molecular mass of SQ-A is reported to be $M_{\text{H}_2} = 0.10 \alpha_{\text{CO}} \times 10^9 M_{\odot}$.

3.5. Neighboring galaxies

The MeerKAT observations also detect HI emission from sixteen neighboring galaxies with radial velocities in the range $5400-7400 \text{ km s}^{-1}$. Their column density, first-order and second-order moment maps are presented in Figures A.4 to A.7. In Table A1, we summarize their properties and optical IDs. Among them, Anon 1, Anon 2, Anon 4, Anon 6, and Anon 8 were reported in previous observations (Shostak 1974; Williams et al. 2002; Xu et al. 2022; Cheng et al. 2023). The remaining eleven sources in the SQ field are either new detections, or new interferometric detections, having been previously identified in large single-dish surveys.

The MeerKAT derived radial velocities of Anon 1, Anon 2, Anon 4, Anon 6 and Anon 8 are consistent with previous studies (Williams et al. 2002; Cheng et al. 2023). For the newly detected source NGC 7320C, the radial velocity of 6520 km s^{-1} corresponds to a redshift of $z=0.0218$, in rough agreement with optical measurements from Sulentic et al. (2001) and Duarte Puertas et al. (2019), but conflicting with the $\sim 6000 \text{ km s}^{-1}$ fiducial redshift in the NASA/IPAC Extragalactic Database (NED) and Lyon Extragalactic Data Archive (LEDA⁸). The optical redshift of NGC 7320B (S1) implies a velocity of 6380 km s^{-1} which is comparable to the HI velocity of 6359 km s^{-1} . Anon5 was reported by Shostak (1974) as a single HI source with a radial velocity of 6115 km s^{-1} and a velocity width of 353 km s^{-1} . In the same region, the MeerKAT data resolve the HI emission into two separate sources (S3 and S9), both with optical counterparts. The majority of the galaxies show velocity distributions consistent with rotation, but S3 and S9 are asymmetric and may be HI tails. Sources S7 and S8 also appear somewhat disturbed, with multiple optical/IR sources within the HI contours, possibly indicating tidal interactions.

3.6. Summary of key results

As described above, the MeerKAT data reveals significant additional HI in SQ compared to past interferometric observations, confirming the basic structure described by Williams et al. (2002) but identifying a number of important new features. New findings from these observations include:

1. The first detection of HI associated with member galaxies NGC 7319 and NGC 7302C,
2. Detection of significant additional emission in the north of NGC 7318B and between NGC 7318B and NGC 7319. In integrated maps, these galaxies are encompassed by a single ~ 70 kpc wide HI structure, with total HI mass a factor >3 times greater than that found from the VLA.
3. Identification of the spatial location of the 6300 and 6900 km s^{-1} HI components previously found in FAST spectra. The 6900 km s^{-1} component is centered around the position of the SQ-A starburst, while the 6300 km s^{-1} component is found along lines of sight through the north of NGC 7318B and between NGC 7318B and NGC 7319.
4. Recovery of the majority ($\sim 80\%$) of the HI emission found by single dish observations, suggesting that MeerKAT is likely capturing all the major HI structure in SQ.

⁸ <http://leda.univ-lyon1.fr/>

In the following section we will consider these results in the context of past work on SQ and examine their implications for the dynamics and internal structure of the group.

4. DISCUSSION

4.1. Comparison with other wavelengths

Given the additional HI identified by MeerKAT, it seems worthwhile to re-examine the relationship between this neutral atomic material and other structures in SQ. Figure 8 (upper-left panel) provides a comparison between the HI distribution in the 6600 component and the radio continuum emission in the group, dominated by the roughly S-shaped shock ridge. Previous studies established that this ridge connected the massive HI component around SQ-A to the base of the southern HI tail behind NGC 7320. This connection is thought to trace the line of a tidal gas filament that once included both the southern HI tail and the high-velocity ($>6500 \text{ km s}^{-1}$) gas around SQ-A and NGC 7319.

If we consider the summed MeerKAT HI map (Figure 4), much of the gap in the HI emission along the shock ridge reported by, e.g., Williams et al. (2002) now appears to be filled in, with only a smaller HI-free region extending northwest from NGC 7320 toward the nucleus of NGC 7318B, crossing the southeast arm of the latter galaxy on its way. As shown in Figure 6 top-panel, much of the new HI emission along the shock ridge is found at low velocities ($5650\text{--}6200 \text{ km s}^{-1}$). This material seems to be associated with NGC 7318B and (in part) the southern bridge structure. At higher velocities, less HI is found in the ridge, and the southern half of the ridge appears to contain no HI at velocities $>6200 \text{ km s}^{-1}$ (Figures 7 and 8). Interestingly, the southern half of the shock ridge shows the brightest radio emission. A detailed comparison of the radio continuum emission with the HI is presented in paper II.

Figure 8 also shows comparisons of the 6600 km s^{-1} HI component with the shock region as traced in soft X-rays by *Chandra* and in the infrared by *JWST* MIRI. The X-ray emission traces the same S-shaped structure seen in the radio continuum emission: the main ridge runs north-south between roughly R.A. = $22^{\text{h}}36^{\text{m}}00^{\text{s}}$, Dec. = $33^{\circ}58'40''$ and Dec. = $33^{\circ}57'30''$, its northern end turns northwest across SQ-A, while the southern end of the ridge turns southeast and splits into two branches. These branches seem to wrap around the base of the HI tail (behind NGC 7320). The *Chandra* image also shows two filaments extending northeast from the ridge, one connecting to the nucleus of NGC 7319, the other toward its northern edge; we have labeled these as X-ray bridge south and north respectively. These two "bridge" structures have been identified previously from $\text{H}\alpha$ emission (e.g., Sulentic et al. 2001; Duarte Puertas et al. 2019) indicating the presence of warm $\sim 10^4 \text{ K}$ ionized gas as well as the $\sim 10^7 \text{ K}$ thermal plasma seen by *Chandra*.

The *JWST* MIRI (Pontoppidan et al. 2022; Pontoppidan & Gordon 2022) bands all contain infrared continuum emission, but (as discussed by Appleton et al. 2023) the $10\mu\text{m}$ band (emission in green) also contains the relatively strong H_2 0-0 S(3) emission line tracing warm molecular hydrogen. The $7.7\mu\text{m}$ band (emission in blue) has a weaker contribution from H_2 line emission and polycyclic aromatic hydrocarbon (PAH) emission, the latter being a good tracer of star formation. Blue and white regions, therefore, probably trace star formation and dust emission, while green regions are more likely to be dominated by H_2 emission. The $10\mu\text{m}$ is strong in the northern half of the ridge up to SQ-A, and in the southern bridge. Interestingly, in the southern half of the ridge, the $10\mu\text{m}$ emission follows the path of the radio continuum and X-ray emission, running north-south until it turns southeast and branches at the base of the HI tail. In contrast, emission in the 7.7 and $15\mu\text{m}$ bands traces the southeast spiral arm, crossing the ridge twice as the arm curves out eastward from the galaxy core, and then around to the southwest. This difference is also seen in the $\text{H}\alpha$, with the shocked, high velocity-dispersion gas following the north-south ridge, while the low velocity-dispersion emission from HII regions follows the southeast spiral arm (Duarte Puertas et al. 2019; Arnaudova et al. 2024). It therefore seems that the radio continuum, X-ray, H_2 and $\text{H}\alpha$ line emission are all tracing different aspects of the same shocked material.

The MeerKAT data shows the presence of HI along the line of sight to the northern part of the shock ridge at a range of velocities, including the high-velocity (6600, 6900) components which the pre-shock tidal filament may have connected to, and (in smaller quantities, closer to SQ-A) in the $6200\text{--}6500 \text{ km s}^{-1}$ range that the shocked ionized component occupies (Figure 6). This suggests that at least some HI has survived the collisional shock or has been able to rapidly cool in this region, despite the harsh conditions. The southern bridge has been shown to contain both warm and cold molecular gas (Appleton et al. 2023; Emonts et al. 2025), the MeerKAT data shows it also contains HI, and we also see both X-ray and radio continuum emission. By contrast, the northern bridge is a much less coherent structure. The X-ray bridge runs along the inner edge of the HI bridge, neither component shows strong $10\mu\text{m}$ emission in the MIRI image, and while there is diffuse radio emission in the region, there is no clear separate radio structure associated with the bridge. The ACA did not detect CO(2-1) emission in the northern bridge, but new ALMA CO(2-1) observations do (Appleton, priv. comm.). We discuss the bridges in more detail in Section 4.5.

4.2. The tidal tails and NGC 7320C

The MeerKAT view of the HI tail structures agrees well with that found by the VLA, while adding some additional detail. It has been suggested that the optical and HI tails

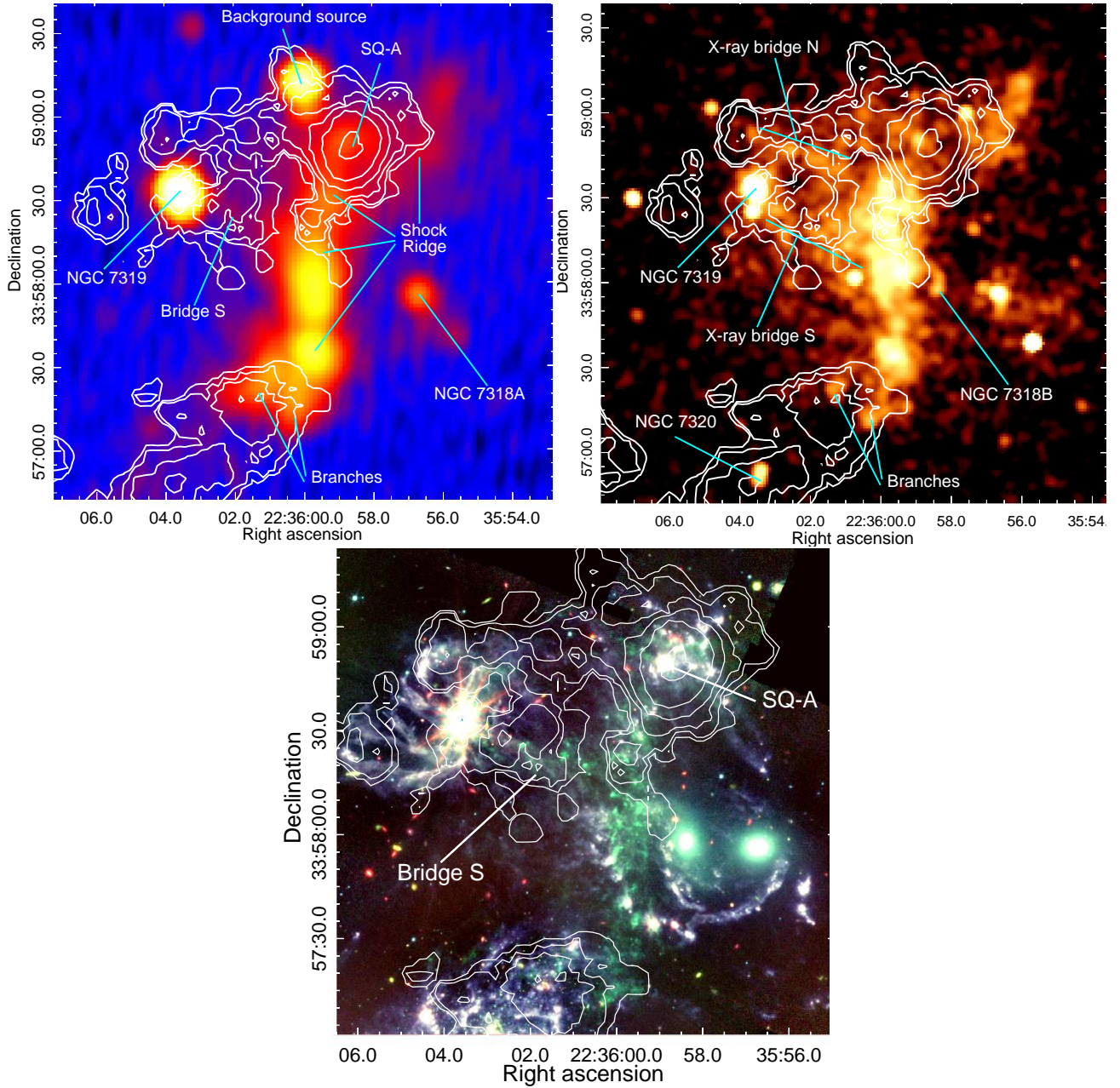


Figure 8. *Upper Left:* MeerKAT $8''$ resolution L-band continuum image of the group core. Labels indicate main shock ridge, the active nuclei of two of the member galaxies, the southern bridge linking the shock to NGC 7319, and other features. *Upper Right:* *Chandra* 0.3-2 keV image of the group core, smoothed with a $3''$ Gaussian. Note the two filamentary X-ray bridges linking the shock ridge to NGC 7319. *Lower:* *JWST* MIRI false colour image of the group core with F1500W/F1000W/F770W images providing the red/green/blue channels. Note the green $10\mu\text{m}$ emission running vertically north-south along the shock ridge, and along the southern bridge to NGC 7319. All three images have MeerKAT HI $6500\text{-}6800\text{ km s}^{-1}$ contours overlaid.

might have been drawn out by the passage of NGC 7320C through the group (Moles et al. 1998; Sulentic et al. 2001), and deep optical imaging (e.g., Duc et al. 2018; Duarte Puer-tas et al. 2019) reveals low surface brightness filaments connecting the optical tails (particularly arc-S) to NGC 7320C. Our MeerKAT observations reveal HI in the disk of that galaxy for the first time, and while it appears morphologically disturbed, it also shows a velocity gradient indicative of

rotation, suggesting the gas is still bound. However, we do not see any direct connection to the HI tails. Instead, arc-N extends $\sim 2.5'$ ($\sim 68\text{ kpc}$) north of SQ-B, along a path traced by much fainter optical filaments.

The velocity distribution is flat over most of the arc, and the velocity dispersion is low ($10\text{-}30\text{ km s}^{-1}$) as expected for tidal structures (Figure 7 top panel). We observe the same velocity gradient in the base of the arc-S (behind NGC 7320) re-

ported by Williams et al. (2002) with velocities increasing to $\sim 6750 \text{ km s}^{-1}$. The tails are thought to have once been connected to the northern high-velocity (6600, 6900) HI components through what is now the shock ridge, and it is unclear whether this velocity gradient would have continued along this pre-existing filament. Without such a gradient, the tails would have connected to the more massive $\sim 6600 \text{ km s}^{-1}$ northern component; with a constant gradient, the tails would instead connect to the $\sim 6900 \text{ km s}^{-1}$ component. The presence of such a velocity gradient could have implications for the formation of the pre-collision filament.

The highest column densities ($8.4 \times 10^{20} \text{ atoms/cm}^2$) in the tails are found where arc-N overlaps the optical tail east of SQ-B. Previous CO observations have shown that $\sim 4 \times 10^8 M_{\odot}$ of molecular gas is located in SQ-B and the smaller star formation region at the end of the optical tail (SQ-tip, Lisenfeld et al. 2002, 2004). This is comparable to the HI mass in the region, $5.0 \pm 0.4 \times 10^8 M_{\odot}$. The CO mean velocity, 6625 km s^{-1} is in excellent agreement with the HI (see Figure A.3). We see no change in HI velocity structure in these regions; the mean velocity remains flat along the tail, and there is no obvious change in velocity dispersion. More diffuse molecular gas is likely present in much of the younger, northern tail (Maeda et al. 2025) with a total mass of $1.85 \times 10^9 M_{\odot}$ (corrected to our adopted distance). This is around 30% of the HI mass we find in the northern tail with MeerKAT.

4.3. The low-velocity component and NGC 7318B

Opinion has varied on the question of how much HI is still associated with the disk of the intruder galaxy, NGC 7318B. Moles et al. (1997, 1998) argued that the 5700 and 6000 km s^{-1} components found by the Westerbork Synthesis Radio Telescope were best interpreted as HI in the galaxy disk, with a central hole corresponding to the nuclear bulge of the galaxy. However, Williams et al. (2002) found a significant spatial gap ($\sim 15\text{-}45''$ or $\sim 7\text{-}21 \text{ kpc}$) between the two HI components, as well as the 300 km s^{-1} difference in velocity. They argued that no plausible mechanism could produce such a separation, and concluded that only the 5700 km s^{-1} component was still associated with the galaxy disk.

MeerKAT shows that HI in the 5700 and 6000 km s^{-1} components does in fact cover much of the spatial extent of the disk of NGC 7318B, though there are still gaps in the galaxy core, the disk just north of the core, and in the southeast quadrant (see Figure 6, or Figure A.1 for a combined moment 0 map). The velocities of the two components overlap in the central regions where little HI was detected by the VLA and the overall velocity structure is consistent with disk rotation; we see the lowest velocities in the south, the highest in the north, and intermediate velocities to east and west

of the galaxy core, with opposite velocity gradients in the north and south implying clockwise rotation. This would be consistent with the direction of curvature of the optical spiral arms. The relative velocity difference between north and south is $\sim 300 \text{ km s}^{-1}$. Yttergren et al. (2021) reported a stellar velocity gradient with a similar alignment, though their data only cover a northeast-southwest band centered on the galaxy core, and only show a relative velocity difference of $\sim 240 \text{ km s}^{-1}$. $\text{H}\alpha$ measurements show ionized gas at similar velocities to the HI in SQ-A, and in NGC 7318B's northeast and southeast arms (Duarte Puertas et al. 2019).

The HI spatial distribution is ellipsoidal, generally consistent with the optical and implying a disk with significant inclination to the line of sight. Adopting the optical inclination of 58.4° (Makarov et al. 2014) the true disk rotational velocity would be $\sim 175 \text{ km s}^{-1}$, not unreasonable for a relatively small spiral such as NGC 7318B. The total mass of HI in the low velocity (5700+6000) components is $6.9 \times 10^9 M_{\odot}$, about 53% of the predicted HI mass for the galaxy based on its luminosity (Jones et al. 2023). If we accept these components as a disk, the rotational velocity suggests a total gravitational mass of $\sim 3 \times 10^{11} M_{\odot}$ within a radius of 41 kpc ($1.5'$). The HI would thus make up $\sim 2\%$ of the total mass within this radius.

However, there is a distinct offset between the HI velocities in the north and the optical recession velocity of the galaxy ($5774 \pm 24 \text{ km s}^{-1}$, Hickson et al. 1992). This could indicate that the disk rotation is asymmetrical or the gas is disturbed, or that the northern 6000 km s^{-1} component may not be associated with NGC 7318B. One possibility is that we are seeing the effects of a collision between the disk of NGC 7318B and the higher-velocity HI components along the line of sight through SQ-A. This collision might have driven gas out of the disk, decelerating it compared to the stars. It is notable that the gas in the 6000 km s^{-1} component follows the optical arms in the north of NGC 7318B, and thus must have interacted with the higher-velocity gas if NGC 7318B is moving along the line of sight.

4.4. The high-velocity components: NGC 7319 and SQ-A

As noted previously, the VLA observations found the northern $\sim 6600 \text{ km s}^{-1}$ HI component to be centered around the SQ-A starburst region, with no emission observed in NGC 7319 or between the galaxies (Williams et al. 2002). The MeerKAT data show significant additional structure (Figures 6 and 7). Firstly, the HI associated with SQ-A is now revealed to have a previously unknown, relatively compact $\sim 6900 \text{ km s}^{-1}$ component. Secondly, the known $\sim 6600 \text{ km s}^{-1}$ component is much more extended than the VLA data suggested, with significant emission in the disk of NGC 7319 and a bridge linking the north-western edge of that galaxy to SQ-A (Fig. 7).

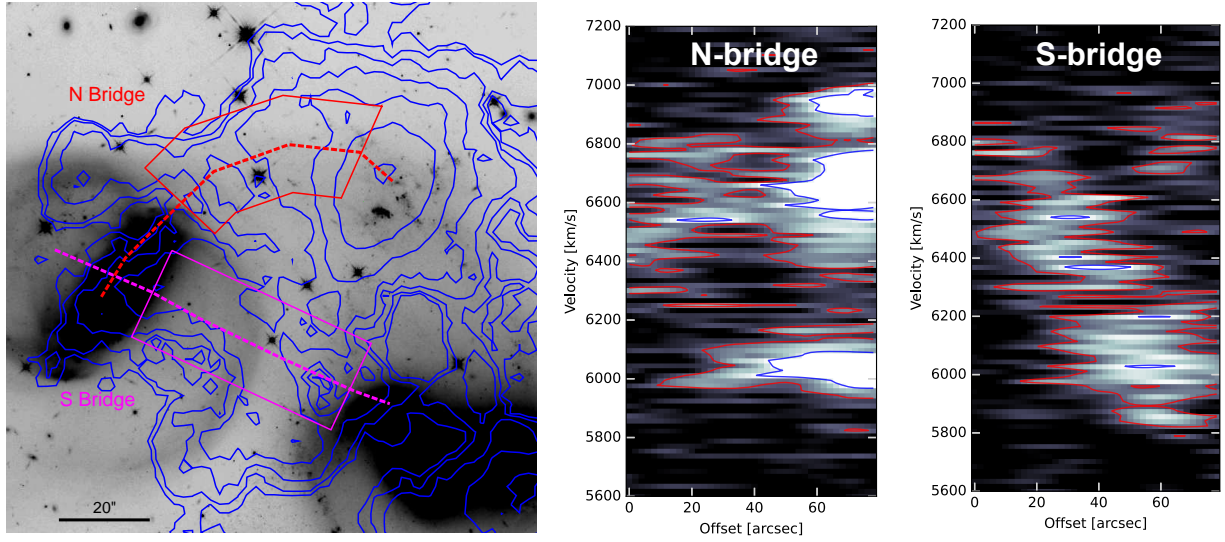


Figure 9. Segmented position-velocity diagrams of the northern (middle panel) and southern (right panel) bridges in HCG92, with red and blue contours showing H I emission at 3 and 6 times the rms noise, respectively. In the left panel, dashed lines show the paths used to extract the PV diagrams, overlaid on the *HST* F140W image, with total ($5560\text{--}7050\text{ km s}^{-1}$) HI contours overlaid in blue. Box regions show the $21''$ width of the PV paths, and indicate the regions considered as bridges. In both center and right panels, the x-axis shows offset from east to west along these paths.

In general, the distribution of the high-velocity HI components in the northern part of the group are suggestive of tidal structures. While HI is seen in NGC 7319 for the first time in modern interferometric observations, its distribution is very lopsided with far more gas on the west side of the galaxy. The newly-identified northern HI bridge linking it to the SQ-A region as well as the previously identified southern bridge linked to NGC 7318B may also suggest that cool gas has been transported westward from the galaxy by tidal interactions. Tidal stripping is common in compact groups (e.g., Verdes-Montenegro et al. 2001b; Konstantopoulos et al. 2010; Borthakur et al. 2010; Jones et al. 2023) and these new structures may well have formed in the interactions which produced the tidal tails. Ram-pressure stripping generally has less impact in low-mass groups (Roberts et al. 2021) than in galaxy clusters and is unlikely to be effective on short timescales in the relatively limited IGrM of SQ, except possibly for gas in NGC 7318B, which is moving supersonically compared to that IGrM (O’Sullivan et al. 2009). The peak electron density in the shock ridge is $\sim 2.5 \times 10^{-2}\text{ cm}^{-3}$ (O’Sullivan et al. 2009), but in the surrounding halo densities will be at least two orders of magnitude lower. The hot IGrM is also rather irregular and only detected out to $\sim 100\text{ kpc}$ (Trinchieri et al. 2005; O’Sullivan et al. 2009).

In NGC 7319, the velocity of the HI overlaps the optical recession velocity of the galaxy ($6747 \pm 4\text{ km s}^{-1}$, Nishiura et al. 2000) but the mean HI velocity is $\sim 100\text{ km s}^{-1}$ lower. In the $25''$ resolution maps we see some indications of a velocity gradient, with velocities of $\sim 6750\text{ km s}^{-1}$ on the northeast side of the disk and $\sim 6550\text{ km s}^{-1}$ on the south-

west. This could indicate rotation, but given the evidence of tidal disturbance of the galaxy, and the bridge of HI which links the southwest quadrant of NGC 7319 to NGC 7318B, it seems more likely that the lower velocities arise from unbound or disturbed gas. Yttergren et al. (2021) found an even stronger gradient in ionized gas emission along a similar axis, but noted that the velocity gradient of the stellar component is offset by almost 90° and that the centers of the stellar and gas velocity fields are offset.

Emonts et al. (2025) report CO emission from the nucleus of NGC 7319 and extending along the southeast spiral arm or loop, another clump in the northeast part of this loop, and extending into the bridge structure (discussed below). We see HI clumps on the eastern side of the galaxy overlapping the regions detected in CO, and on the west side extending from the galactic bar down to the bridge (Figure A.3). The CO emission shows the same velocity gradient we observe in the HI, providing evidence that the two gas phases are co-spatial. However, we do not see strong HI emission to match the CO emission from the nuclear region. The bright Seyfert nucleus of NGC 7319 may have played a role in driving out or ionizing low-density atomic gas from the nuclear region (Aoki et al. 1996; Pereira-Santaella et al. 2022). The total molecular mass in the galaxy depends on the assumed CO conversion factor α_{CO} . For the typical value found in the Milky Way ($\alpha_{\text{CO}}=4.6$, Solomon & Vanden Bout 2005) the molecular gas mass would be $\sim 2 \times 10^9 M_\odot$, roughly double the mass of HI observed in the galaxy. This could indicate that past interactions have been more effective in removing low-density material, perhaps because of differences in dis-

tribution; a more extended low-density gas disk might have proven more susceptible to tidal forces. Alternatively, interactions may have caused compression of the HI, leading to the formation of more molecular gas. However, the true value of α_{CO} in NGC 7319 is unknown, and the molecular gas mass could be significantly lower.

4.5. The bridge structures

As noted above, two HI bridge structures link NGC 7319 to NGC 7318B and the SQ-A region. Components of both are visible at multiple frequencies, indicating highly multiphase gas, as in the main shock ridge. While all components of the southern bridge follow a consistent path, in the northern bridge there are differences. The stellar component follows a curved path, with multiple arcs linking the northwest side of NGC 7319 to the northern part of NGC 7318B and SQ-A. In contrast, the northern X-ray bridge and H α emission seem to follow separate but straighter lines, with the X-ray bridge (Figure 8) running roughly southwest-northeast, and the relatively weak H α running east-west (Sulentic et al. 2001; Duarte Puertas et al. 2019). The HI bridge is primarily seen in the 6600 component, linking the region around SQ-A to the northwest edge of NGC 7319 and the HI in the disk of that galaxy. While the emission from the different gas and stellar components overlaps, there are distinct offsets in position, and without velocity measurements we cannot be sure whether the ionized gas and X-ray plasma are cospatial with the HI. The position-velocity (PV) diagram for the northern bridge (Fig. 9 middle-panel) shows no strong evidence of a velocity gradient. In the center of the bridge the HI covers a velocity range $\sim 6500\text{--}6800\text{ km s}^{-1}$, somewhat narrower than the velocity ranges in the galaxies, and there seems to be no connection to the 6900 km s^{-1} component in SQ-A. The 6000 km s^{-1} in northern NGC 7318A/B overlaps the northern bridge but does not extend into NGC 7319. We note that using an east-west route for the northern bridge, between SQ-A and the northeastern-most HI clump in NGC 7319, would not change our conclusions; it shows the same mid-bridge velocity range and the same $>3\sigma$ significant connection at velocities $\sim 6780\text{ km s}^{-1}$, but the northeast clump lacks the emission at ~ 6680 and $\sim 6540\text{ km s}^{-1}$ we see in the central regions of NGC 7319.

The southern bridge has been detected in H α (e.g., Sulentic et al. 2001), H β (Guillard et al. 2022), warm H $_2$ (Cluver et al. 2010; Appleton et al. 2017), [CII] (Appleton et al. 2013) and CO (Guillard et al. 2012) as well as the X-ray and radio continuum emission noted above. Emonts et al. (2025) revealed a strong velocity gradient in the ACA CO(2-1) data for the bridge, with velocities falling by $\sim 700\text{ km s}^{-1}$ over a distance of $\sim 25\text{ kpc}$ from NGC 7319 to the shock ridge. Ionized gas clumps are observed in the bridge at $\sim 6400\text{ km s}^{-1}$ (Konstantopoulos et al. 2010; Duarte Puer-

tas et al. 2019), consistent with the CO velocities. Figure 9 right-panel shows the HI position-velocity diagram along this structure, though covering a broader ($21''$) band than the CO owing to the larger HI beam size. We see the same overall gradient, with velocities falling from $\sim 6600\text{ km s}^{-1}$ in the core of NGC 7319 to $\sim 5900\text{ km s}^{-1}$ at the shoulder of the southeast spiral arm of NGC 7318B. In the CO, separate components are seen in the NGC 7319 nucleus and eastern bridge, merging to form a single structure in the western bridge. We do not observe this in the HI, and while the broader HI beam size might make separation of nucleus and bridge difficult, we see no hints of a broader HI velocity distribution, as might be expected. We do observe some weak (3σ significant) emission clumps apparently unrelated to the bridge in the $\sim 6700\text{--}6900\text{ km s}^{-1}$ range on the western side. These correspond to the small quantities of HI at the group velocity which extend down the shock ridge from SQ-A into the shoulder of the southeast spiral arm, as seen in Fig. 7.

The origin of the two bridges is unclear, and indeed their properties may suggest different formation histories. In the southern bridge, the close correlation of components with very different temperatures suggests that the bridge was originally a cool gas structure which has been shock heated, as is the case for the main shock ridge. However, the fairly strong velocity gradient of the bridge is difficult to explain. While the Seyfert nucleus of NGC 7319 has been shown to be driving outflows (e.g., Aoki et al. 1996) and radio jets (Xanthopoulos et al. 2004) aligned roughly southwest-northeast, their scale ($\sim 2\text{--}5\text{ kpc}$) is much smaller than the bridge and the jet alignment is offset from the bridge by $\sim 40^\circ$. It is also unclear how an outflow could produce the observed velocity gradient, or why it should connect to the velocity of NGC 7318B. At first glance a tidal origin for both bridges seems more plausible, with gas being drawn out of NGC 7319 by the interactions that formed the high-velocity HI components around SQ-A, the older (southern) tidal tail, and the filament which is presumed to have linked them. The relatively flat velocity across the northern bridge would be consistent with an interaction primarily occurring in the plane of the sky. However, the velocity gradient in the southern bridge would then have to be the product of the more recent collision of NGC 7318B with these tidal structures. In this scenario, the differences between the two bridge structures are more difficult to explain; if both are the product of tidal forces and the shock from the collision of NGC 7319, why are their velocity structures different, and why does the northern bridge not show the same coherent multi-wavelength structure seen in the southern bridge?

4.6. Intermediate velocity structures: the shock zone

HI located in the shock ridge at the intermediate ($6200\text{--}6500\text{ km s}^{-1}$, Figure 6 bottom-panel) velocity range is of

particular interest. This is the velocity range in which H α observations find the majority of the shocked, high velocity-dispersion ionized gas (Arnaudova et al. 2024) associated with the shock ridge. This ionized gas seems likely to trace the material most strongly affected by the collisional shock, with its intermediate velocity indicating that it has been accelerated either from the pre-existing tidal HI filament, or out of the disk of NGC 7318B.

Part of the HI flux observed in this component by FAST (Cheng et al. 2023) is now confirmed as arising from gas in the northern shock ridge coincident with the northeast arm of NGC 7318B, and in the northern part of SQ-A (Figure 6 bottom-panel). However, in this velocity component we do not see the strong peak in HI column densities at the position of SQ-A found in the 6000, 6600 and 6900 components. The HI is limited to the northern half of the ridge (as is HI in the 6600 component) avoiding the regions of brightest radio continuum emission in the southern half of the ridge. This could suggest a variation in shock strength from north to south, with stronger shocks in the south effectively ionizing all of the HI in that portion of the tidal filament, while some HI survived the collision in the north. An alternative would be variation in time since collision; if the tidal HI filament were tilted out of the plane of the sky, NGC 7318B might have collided with the northern part first. In this case, the intermediate-velocity HI in the northern ridge might be gas which was initially ionized and accelerated by the collision, but has now had time to cool back into the neutral phase, while retaining its new velocity. Discriminating between these options, or other possible origin scenarios, requires information on shock strength and age. We therefore defer further discussion to paper II, where the results of radio continuum analysis may provide insight.

5. SUMMARY AND CONCLUSIONS

In this work, we have presented MeerKAT (6 hrs on-source) HI observations of SQ. This dataset reveals significant new structure in the atomic gas and provides a clearer view of features identified in earlier studies. With a restoring beam of $17'' \times 14''$ and a smoothed velocity resolution of 16.5 km s^{-1} , we reach a 1σ HI column density sensitivity of $1.3 \times 10^{19} \text{ cm}^{-2}$. Below, we summarize our primary results:

1. We report the first modern interferometric detection of HI emission in NGC 7319, and the first detection of HI in NGC 7320C. In NGC 7319 the bulk of the HI is located in the western disk, with the overall spatial distribution clumpy and asymmetric, and the velocity distribution mildly offset from the stellar component. The HI appears to share a similar distribution to the previously detected molecular gas, except in the galaxy core where CO emission is at its strongest but HI emission is weak. In NGC 7320C we find $\sim 2 \times 10^8 M_{\odot}$

of atomic gas, with a mean velocity of 6520 km s^{-1} ($z=0.0218$) in agreement with past optical measurements (Sulentic et al. 2001; Duarte Puertas et al. 2019). The HI emission extends $\sim 45''$ (20 kpc) north-south, covering the optical disk, and has a velocity gradient suggestive of rotation. We do not find any HI connecting NGC 7320C and the HI tidal tails of SQ.

2. We confirm the previous finding of a large mass of HI emitting gas at the group velocity ($\sim 6600 \text{ km s}^{-1}$) along a line of sight through the northern half of the NGC 7318A/B galaxy pair, peaking close to the position of the starburst region SQ-A. We see significant structure in this gas, with filaments extending along the optical arms of NGC 7318B, including the northern half of the shock region. We determine the location of the high-velocity ($\sim 6900 \text{ km s}^{-1}$) HI emission previously detected in low spatial resolution observations, finding it to be also centered on SQ-A.
3. Our new observations uncover an HI counterpart to the CO/H 2 /H α bridge linking NGC 7319 and NGC 7318B, and show the same $\sim 700 \text{ km s}^{-1}$ velocity gradient along its $\sim 25 \text{ kpc}$ length found in CO emission. This bridge is also detected in X-ray and radio continuum emission. While the origin of the bridge is unclear, its orientation and smooth velocity gradient make it difficult to explain except as a tidal feature.
4. We detect a second HI bridge linking the northwest quadrant of NGC 7319 to SQ-A. It shows a relatively flat velocity distribution at $\sim 6600 \text{ km s}^{-1}$ despite its western end being only $\sim 20 \text{ kpc}$ north of the previously identified southern bridge. Some clumpy CO emission has been found in this northern bridge, and an X-ray filament runs along its southern edge, but there is no clear corresponding radio continuum or warm H 2 structure. If the bridges are tidal structures shocked by the collision of NGC 7318B with the group, this suggests that the north bridge was less affected by the shocks than its southern counterpart.
5. For the HI tidal tails extending east of the group center, the MeerKAT data shows very similar morphology to that found by the VLA. The separation between the northern and southern tails is clearer, with a definite gap in emission between the two. However, we find no evidence for distinct kinematics or separate velocity dispersion.
6. At lower velocities ($\sim 5650\text{-}6200 \text{ km s}^{-1}$) we find the HI emission in and around NGC 7318B is significantly more extended than was suggested by the VLA observations. HI fills much of the area of the disk with

gaps only seen in the galaxy core, in the region immediately north of the core, and in a channel extending southeast across the (CO-rich, star-forming) SE arm of NGC 7318B. The velocity structure of the HI is suggestive of clockwise disk rotation, consistent with the orientation of the spiral arms of NGC 7318B. Taking into account the inclination of the galaxy, the rotational velocity of such a disk would be $\sim 175 \text{ km s}^{-1}$. The total gas mass would be $\sim 3 \times 10^{11} M_{\odot}$ within 41 kpc radius, $\sim 53\%$ of the HI mass expected for NGC 7318B based on its optical luminosity. However, we note that the gas in the northern, $\sim 6000 \text{ km s}^{-1}$ component appears offset from the optical redshift of the galaxy, perhaps indicating disturbance from the interaction with the higher-velocity material around SQ-A.

7. The MeerKAT data confirms the connection between the HI tails and the northern high-velocity ($6600+6900 \text{ km s}^{-1}$) HI structures around SQ-A through the shock ridge. The southern end of the ridge splits into two branches which wrap around the base of the southern HI tail. The brightest radio continuum emission is detected in the southern bridge, where there is little or no HI emission in the group velocity range. By contrast, HI is found in this velocity range in the northern ridge, where the radio continuum emission is fainter and X-ray emission brighter. MeerKAT also localizes some of the intermediate velocity ($6200-6500 \text{ km s}^{-1}$) HI emission previously detected by single-dish measurements, showing it to be in the northern shock ridge, north of SQ-A, and associated with the two HI bridges. This is the velocity range in which shock-excited $H\alpha$ emission dominates, implying that at least some of this HI is associated with gas strongly affected by the collision shock.
8. We measure a total HI integrated flux density of $17.2 \pm 2.0 \text{ Jy km s}^{-1}$ from the combined spectrum of SQ. The corresponding atomic gas mass is $M_{\text{HI}} = 3.5 \pm 0.4 \times 10^{10} M_{\odot}$ for our adopted distance of 94 Mpc. This is slightly lower than, but consistent within uncertainties with, the single-dish measurement from FAST. Based on the spatially masked SoFIA maps, which are more directly comparable with prior interferometric observations, we find a lower integrated flux density of $12 \pm 1 \text{ Jy km s}^{-1}$ ($\geq 3\sigma_{\text{rms}}$), equivalent to an atomic gas mass of $M_{\text{HI}} = 2.4 \pm 0.2 \times$

$10^{10} M_{\odot}$. This is still a factor ~ 1.8 higher than previous VLA estimates. These measurements suggest that MeerKAT is capturing the majority of the HI flux from the group, and therefore probably mapping all the major HI structures.

9. We detected HI emission from sixteen neighboring galaxies in the SQ field, of which eleven are either previously undetected or new interferometric detections.

The new and expanded HI structures identified within the group have implications for our understanding of the galaxy interactions which have brought the group to its current state. Although in this work, we have focused on the HI spectral line, our MeerKAT data also provide an exceptionally sensitive window on the radio continuum emission from the group. In paper II, we will combine the results presented here with a broad-band continuum analysis (144 MHz to 8 GHz), with the goal of providing insight into the dynamics of the group and the formation mechanism of the shock ridge.

ACKNOWLEDGMENTS

The authors thank the staff of the MeerKAT observatory for their help with the observations presented in this work. The MeerKAT telescope is operated by the South African Radio Astronomy Observatory, which is a facility of the National Research Foundation, an agency of the Department of Science, Technology and Innovation. Some of the computations in this paper were conducted on the Smithsonian High Performance Cluster (SI/HPC), Smithsonian Institution (<https://doi.org/10.25572/SIHPC>). Basic research in radio astronomy at the Naval Research Laboratory is supported by 6.1 Base funding. This research has made use of the NASA/IPAC Extragalactic Database, which is funded by the National Aeronautics and Space Administration and operated by the California Institute of Technology. We acknowledge the usage of the HyperLeda database (<http://leda.univ-lyon1.fr>).

Facilities: MeerKAT, CXO

Software: CARACal (Józsa et al. 2020), AOflagger (Offringa et al. 2010), WSClean (Offringa et al. 2014), CARTA (Comrie et al. 2021), DS9 (Joye & Mandel 2003), SoFIA (Serra et al. 2015), Astropy (Astropy Collaboration et al. 2013, 2018), APLpy (Robitaille & Bressert 2012), Matplotlib (Hunter 2007)

REFERENCES

- Allen, R. J., & Hartsuiker, J. W. 1972, *Nature*, 239, 324, doi: [10.1038/239324a0](https://doi.org/10.1038/239324a0)
- Allen, R. J., & Sullivan, III, W. T. 1980, *A&A*, 84, 181
- Aoki, K., Ohtani, H., Yoshida, M., & Kosugi, G. 1996, *AJ*, 111, 140, doi: [10.1086/117767](https://doi.org/10.1086/117767)

- Appleton, P. N., Guillard, P., Boulanger, F., et al. 2013, *ApJ*, 777, 66, doi: [10.1088/0004-637X/777/1/66](https://doi.org/10.1088/0004-637X/777/1/66)
- Appleton, P. N., Guillard, P., Togi, A., et al. 2017, *ApJ*, 836, 76, doi: [10.3847/1538-4357/836/1/76](https://doi.org/10.3847/1538-4357/836/1/76)
- Appleton, P. N., Guillard, P., Emonts, B., et al. 2023, *ApJ*, 951, 104, doi: [10.3847/1538-4357/accc2a](https://doi.org/10.3847/1538-4357/accc2a)
- Arnudova, M. I., Das, S., Smith, D. J. B., et al. 2024, *MNRAS*, 535, 2269, doi: [10.1093/mnras/stae2235](https://doi.org/10.1093/mnras/stae2235)
- Aromal, P., Gallagher, S. C., Fedotov, K., et al. 2025, *ApJ*, 994, 90, doi: [10.3847/1538-4357/ae0cb4](https://doi.org/10.3847/1538-4357/ae0cb4)
- Astropy Collaboration, Robitaille, T. P., Tollerud, E. J., et al. 2013, *A&A*, 558, A33, doi: [10.1051/0004-6361/201322068](https://doi.org/10.1051/0004-6361/201322068)
- Astropy Collaboration, Price-Whelan, A. M., Sipőcz, B. M., et al. 2018, *AJ*, 156, 123, doi: [10.3847/1538-3881/aabc4f](https://doi.org/10.3847/1538-3881/aabc4f)
- Balkowski, C., Bottinelli, L., Chamaroux, P., Gouguenheim, L., & Heidmann, J. 1973, *A&A*, 25, 319
- Borthakur, S., Yun, M. S., & Verdes-Montenegro, L. 2010, *ApJ*, 710, 385, doi: [10.1088/0004-637X/710/1/385](https://doi.org/10.1088/0004-637X/710/1/385)
- Borthakur, S., Yun, M. S., Verdes-Montenegro, L., et al. 2015, *ApJ*, 812, 78, doi: [10.1088/0004-637X/812/1/78](https://doi.org/10.1088/0004-637X/812/1/78)
- Briggs, D. S. 1995, PhD thesis, New Mexico Institute of Mining and Technology
- Cheng, C., Xu, C. K., Appleton, P. N., et al. 2023, *ApJ*, 954, 74, doi: [10.3847/1538-4357/ace03e](https://doi.org/10.3847/1538-4357/ace03e)
- Cluver, M. E., Appleton, P. N., Boulanger, F., et al. 2010, *ApJ*, 710, 248, doi: [10.1088/0004-637X/710/1/248](https://doi.org/10.1088/0004-637X/710/1/248)
- Comrie, A., Wang, K.-S., Hsu, S.-C., et al. 2021, CARTA: The Cube Analysis and Rendering Tool for Astronomy, 2.0.0, Zenodo, doi: [10.5281/zenodo.4905459](https://doi.org/10.5281/zenodo.4905459)
- Duarte Puertas, S., Iglesias-Páramo, J., Vilchez, J. M., et al. 2019, *A&A*, 629, A102, doi: [10.1051/0004-6361/201935686](https://doi.org/10.1051/0004-6361/201935686)
- Duc, P.-A., Cuillandre, J.-C., & Renaud, F. 2018, *MNRAS*, 475, L40, doi: [10.1093/mnras/sly004](https://doi.org/10.1093/mnras/sly004)
- Emonts, B. H. C., Appleton, P. N., Lisenfeld, U., et al. 2025, *ApJ*, 978, 111, doi: [10.3847/1538-4357/ad957c](https://doi.org/10.3847/1538-4357/ad957c)
- Guillard, P., Boulanger, F., Pineau des Forêts, G., et al. 2012, *ApJ*, 749, 158, doi: [10.1088/0004-637X/749/2/158](https://doi.org/10.1088/0004-637X/749/2/158)
- Guillard, P., Appleton, P. N., Boulanger, F., et al. 2022, *ApJ*, 925, 63, doi: [10.3847/1538-4357/ac313f](https://doi.org/10.3847/1538-4357/ac313f)
- Haynes, M. P., Giovanelli, R., Kent, B. R., et al. 2018, *ApJ*, 861, 49, doi: [10.3847/1538-4357/aac956](https://doi.org/10.3847/1538-4357/aac956)
- Hickson, P. 1982, *ApJ*, 255, 382
- Hickson, P., Mendes de Oliveira, C., Huchra, J. P., & Palumbo, G. G. 1992, *ApJ*, 399, 353, doi: [10.1086/171932](https://doi.org/10.1086/171932)
- Hunter, J. D. 2007, *Computing in Science & Engineering*, 9, 90, doi: [10.1109/MCSE.2007.55](https://doi.org/10.1109/MCSE.2007.55)
- Jones, M. G., Verdes-Montenegro, L., Moldon, J., et al. 2023, *A&A*, 670, A21, doi: [10.1051/0004-6361/202244622](https://doi.org/10.1051/0004-6361/202244622)
- Joye, W. A., & Mandel, E. 2003, in *Astronomical Society of the Pacific Conference Series*, Vol. 295, *Astronomical Data Analysis Software and Systems XII*, ed. H. E. Payne, R. I. Jedrzejewski, & R. N. Hook, 489
- Józsa, G. I. G., White, S. V., Thorat, K., et al. 2020, CARACal: Containerized Automated Radio Astronomy Calibration pipeline, Astrophysics Source Code Library, record ascl:2006.014. <http://ascl.net/2006.014>
- Kenyon, J. S., Smirnov, O. M., Grobler, T. L., & Perkins, S. J. 2018, *MNRAS*, 478, 2399, doi: [10.1093/mnras/sty1221](https://doi.org/10.1093/mnras/sty1221)
- Konstantopoulos, I. S., Gallagher, S. C., Fedotov, K., et al. 2010, *ApJ*, 723, 197, doi: [10.1088/0004-637X/723/1/197](https://doi.org/10.1088/0004-637X/723/1/197)
- Leroy, A. K., Walter, F., Brinks, E., et al. 2008, *AJ*, 136, 2782, doi: [10.1088/0004-6256/136/6/2782](https://doi.org/10.1088/0004-6256/136/6/2782)
- Lisenfeld, U., Braine, J., Duc, P.-A., et al. 2004, *A&A*, 426, 471, doi: [10.1051/0004-6361:20041330](https://doi.org/10.1051/0004-6361:20041330)
- . 2002, *A&A*, 394, 823, doi: [10.1051/0004-6361:20021232](https://doi.org/10.1051/0004-6361:20021232)
- Maeda, F., Komugi, S., Muraoka, K., et al. 2025, *ApJ*, 990, 221, doi: [10.3847/1538-4357/adfc56](https://doi.org/10.3847/1538-4357/adfc56)
- Makarov, D., Prugniel, P., Terekhova, N., Courtois, H., & Vauglin, I. 2014, *A&A*, 570, A13, doi: [10.1051/0004-6361/201423496](https://doi.org/10.1051/0004-6361/201423496)
- Moles, M., Marquez, I., & Sulentic, J. W. 1998, *A&A*, 334, 473
- Moles, M., Sulentic, J. W., & Marquez, I. 1997, *ApJ*, 485, L69, doi: [10.1086/310817](https://doi.org/10.1086/310817)
- Nishiura, S., Shimada, M., Ohyama, Y., Murayama, T., & Taniguchi, Y. 2000, *AJ*, 120, 1691, doi: [10.1086/301561](https://doi.org/10.1086/301561)
- Offringa, A. R., de Bruyn, A. G., Biehl, M., et al. 2010, *MNRAS*, 405, 155, doi: [10.1111/j.1365-2966.2010.16471.x](https://doi.org/10.1111/j.1365-2966.2010.16471.x)
- Offringa, A. R., McKinley, B., Hurley-Walker, N., et al. 2014, *MNRAS*, 444, 606, doi: [10.1093/mnras/stu1368](https://doi.org/10.1093/mnras/stu1368)
- O'Sullivan, E., Giacintucci, S., Vrtilik, J. M., Raychaudhury, S., & David, L. P. 2009, *ApJ*, 701, 1560, doi: [10.1088/0004-637X/701/2/1560](https://doi.org/10.1088/0004-637X/701/2/1560)
- Pereira-Santaella, M., Álvarez-Márquez, J., García-Bernete, I., et al. 2022, *A&A*, 665, L11, doi: [10.1051/0004-6361/202244725](https://doi.org/10.1051/0004-6361/202244725)
- Pontoppidan, K. M., & Gordon, K. 2022, Data from the JWST/ERO program, STScI/MAST, doi: [10.1709/67ft-nb86](https://doi.org/10.1709/67ft-nb86)
- Pontoppidan, K. M., Barrientes, J., Blome, C., et al. 2022, *ApJL*, 936, L14, doi: [10.3847/2041-8213/ac8a4e](https://doi.org/10.3847/2041-8213/ac8a4e)
- Roberts, I. D., van Weeren, R. J., McGee, S. L., et al. 2021, *A&A*, 652, A153, doi: [10.1051/0004-6361/202141118](https://doi.org/10.1051/0004-6361/202141118)
- Robitaille, T., & Bressert, E. 2012, APLpy: Astronomical Plotting Library in Python. <http://ascl.net/1208.017>
- Schruba, A., Leroy, A. K., Walter, F., et al. 2011, *AJ*, 142, 37, doi: [10.1088/0004-6256/142/2/37](https://doi.org/10.1088/0004-6256/142/2/37)
- Serra, P., Westmeier, T., Giese, N., et al. 2015, *MNRAS*, 448, 1922, doi: [10.1093/mnras/stv079](https://doi.org/10.1093/mnras/stv079)
- Shostak, G. S. 1974, *ApJ*, 187, 19, doi: [10.1086/152584](https://doi.org/10.1086/152584)
- Shostak, G. S., Sullivan, III, W. T., & Allen, R. J. 1984, *A&A*, 139, 15

- Solomon, P. M., & Vanden Bout, P. A. 2005, *ARA&A*, 43, 677, doi: [10.1146/annurev.astro.43.051804.102221](https://doi.org/10.1146/annurev.astro.43.051804.102221)
- Springob, C. M., Haynes, M. P., Giovanelli, R., & Kent, B. R. 2005, *ApJS*, 160, 149, doi: [10.1086/431550](https://doi.org/10.1086/431550)
- Stephan, M. 1877, *MNRAS*, 37, 334
- Sulentic, J. W., Rosado, M., Dultzin-Hacyan, D., et al. 2001, *AJ*, 122, 2993, doi: [10.1086/324455](https://doi.org/10.1086/324455)
- Trinchieri, G., Sulentic, J., Breitschwerdt, D., & Pietsch, W. 2003, *A&A*, 401, 173, doi: [10.1051/0004-6361:20030108](https://doi.org/10.1051/0004-6361:20030108)
- Trinchieri, G., Sulentic, J., Pietsch, W., & Breitschwerdt, D. 2005, *A&A*, 444, 697, doi: [10.1051/0004-6361:20052910](https://doi.org/10.1051/0004-6361:20052910)
- van der Hulst, J. M., & Rots, A. H. 1981, *AJ*, 86, 1775, doi: [10.1086/113060](https://doi.org/10.1086/113060)
- Verdes-Montenegro, L., Yun, M. S., Williams, B. A., et al. 2001a, *A&A*, 377, 812, doi: [10.1051/0004-6361:20011127](https://doi.org/10.1051/0004-6361:20011127)
- . 2001b, *A&A*, 377, 812, doi: [10.1051/0004-6361:20011127](https://doi.org/10.1051/0004-6361:20011127)
- Williams, B. A., Yun, M. S., & Verdes-Montenegro, L. 2002, *AJ*, 123, 2417, doi: [10.1086/339839](https://doi.org/10.1086/339839)
- Xanthopoulos, E., Muxlow, T. W. B., Thomasson, P., & Garrington, S. T. 2004, *MNRAS*, 353, 1117, doi: [10.1111/j.1365-2966.2004.08133.x](https://doi.org/10.1111/j.1365-2966.2004.08133.x)
- Xu, C., Sulentic, J. W., & Tuffs, R. 1999, *ApJ*, 512, 178, doi: [10.1086/306771](https://doi.org/10.1086/306771)
- Xu, C. K., Lu, N., Condon, J. J., Dopita, M., & Tuffs, R. J. 2003, *ApJ*, 595, 665, doi: [10.1086/377445](https://doi.org/10.1086/377445)
- Xu, C. K., Cheng, C., Appleton, P. N., et al. 2022, *Nature*, 610, 461, doi: [10.1038/s41586-022-05206-x](https://doi.org/10.1038/s41586-022-05206-x)
- Xu, C. K., Cheng, C., Yun, M. S., et al. 2025, *ApJ*, 991, 197, doi: [10.3847/1538-4357/adfbf6](https://doi.org/10.3847/1538-4357/adfbf6)
- Yttergren, M., Misquitta, P., Sánchez-Monge, Á., et al. 2021, *A&A*, 656, A83, doi: [10.1051/0004-6361/202040188](https://doi.org/10.1051/0004-6361/202040188)

APPENDIX

Table A1. Neighboring Galaxies Detected with MeerKAT in H I

ID	R.A.	Decl.	H I Velocity	Flux density	M_{HI}	Optical/IR ID	References
	(J2000)	(J2000)	(km s^{-1})	(Jy kms^{-1})	($\times 10^9 M_{\odot}$)		
Anon 1	22:35:41.3	+34:16:01	6254	0.50 ± 0.05	1.02 ± 1.00	WISEA J223541.84+341601.6	1,4
Anon 2	22:35:50.4	+34:09:30	6377	0.38 ± 0.04	0.78 ± 0.08	SDSS J223550.70+340930.8	1,2,3,4
Anon 4	22:36:40.4	+33:56:56	6064	0.93 ± 0.10	1.90 ± 0.40	SDSS J223640.85+335654.5	1,2,3,4
Anon 6	22:37:13.8	+34:05:06	6072	0.82 ± 0.10	1.67 ± 0.20	WISEA J223712.99+340508.9	2, 4
Anon 8	22:35:47.5	+34:06:48	5724	0.67 ± 0.06	0.14 ± 0.01	SDSS J223547.54+340648.1	3
NGC 7320C	22:36:20.7	+33:59:09	6520	0.098 ± 0.01	0.20 ± 0.02	NGC 7320C	-
S1	22:37:26.9	+33:55:25	6359	0.78 ± 0.08	1.60 ± 0.20	NGC 7320B	4
S2	22:36:47.7	+33:41:26	6818	0.72 ± 0.08	1.47 ± 0.02	WISEA J223648.42+334131.3	-
S3	22:38:49.9	+34:18:32	6267	0.053 ± 0.005	0.11 ± 0.01	UGC 12132	1,4,5
S4	22:37:25.8	+34:22:02	6628	0.38 ± 0.04	0.78 ± 0.08	NGC 7337	4
S5	22:34:36.2	+33:40:06	6300	0.31 ± 0.03	0.63 ± 0.06	WISEA J223437.66+334006.3	-
S6	22:34:31.1	+33:52:38	5966	0.39 ± 0.04	0.78 ± 0.08	WISEA J223431.13+335250.2	-
S7	22:36:59.4	+33:49:56	7278	0.13 ± 0.01	0.26 ± 0.02	WISEA J223659.36+334948.7	-
S8	22:35:26.3	+34:08:37	6075	0.48 ± 0.05	0.98 ± 0.10	SDSS J223526.26+340837.9	-
S9	22:38:40.0	+34:20:02	6332	0.31 ± 0.03	0.63 ± 0.06	WISEA J223840.57+342016.3	-
S10	22:38:34.3	+34:04:12	7450	2.25 ± 0.20	4.59 ± 0.41	NGC 7343	5

References—prior H I detections: 1: Shostak et al. (1984) 2: Williams et al. (2002), 3: Xu et al. (2022); Cheng et al. (2023), 4: Haynes et al. (2018), 5: Springob et al. (2005)

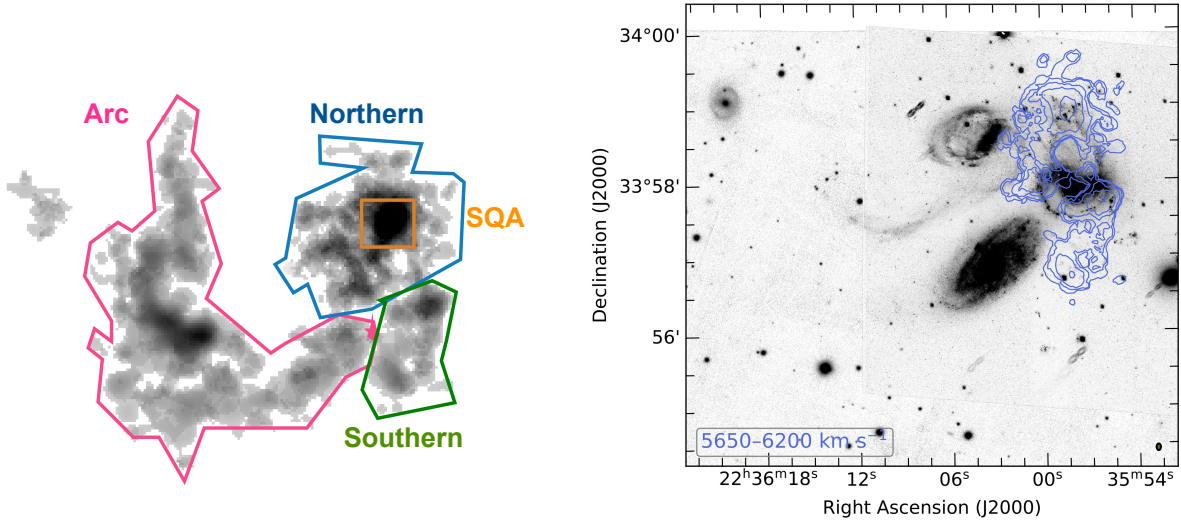


Figure A.1. *Left:* MeerKAT medium resolution ($17'' \times 14''$) total intensity H I map superimposed with regions used to extract the spectra shown in Figure 5. To measure the total integrated flux density of Arc, Northern and Southern regions we used the low resolution map (i.e., $25''$ beam size). *Right:* MeerKAT moment-zero map of the combined 5700 and 6000 km s^{-1} components. H I contour levels are plotted at $5.6, 11.1, 22.3, 44.5, 89.1, 178, \dots \times 10^{19} \text{ atoms cm}^{-2}$. The radio beam size is $17'' \times 14''$.

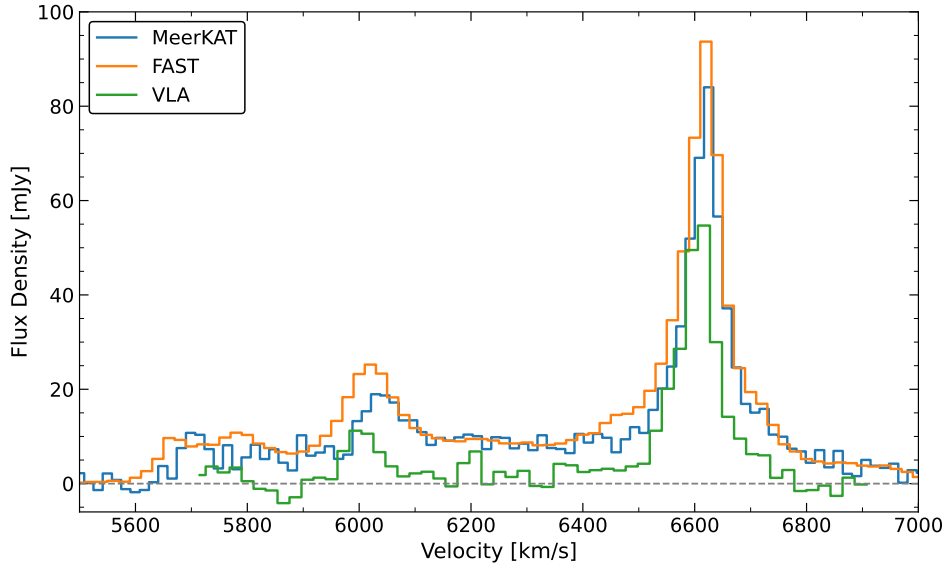


Figure A.2. Comparison of MeerKAT, FAST (Cheng et al. 2023) and VLA (Jones et al. 2023) integrated HI spectra for SQ. The overall HI profile shape for obtained from MeerKAT is similar to that measured by FAST. The dashed gray horizontal line indicates the zero flux density level.

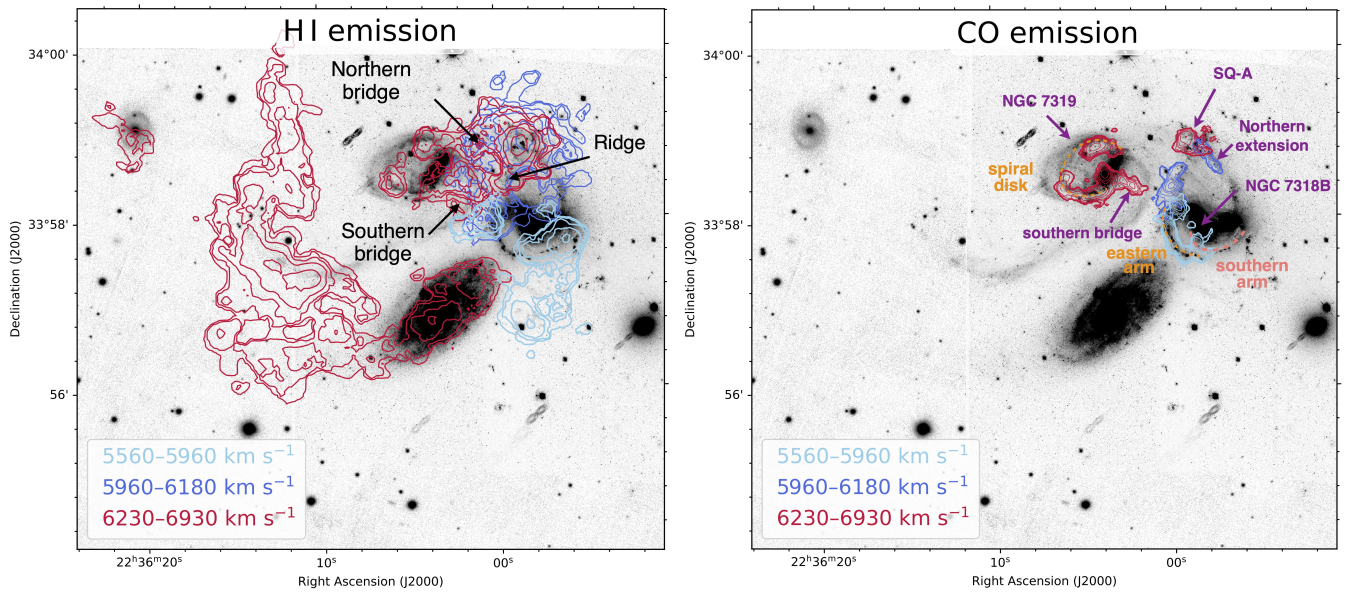


Figure A.3. Kinematic structures of the atomic and cold molecular gases in SQ. The MeerKAT HI (left) and CO (right) emission are superimposed on the HST+DSS optical image, integrated across three velocity range. The HI contours are same as in Figure 3. The CO(2-1) contours are from Atacama Compact Array with the beam size $8'' \times 7''$ (adopted from Emonts et al. 2025). The CO contours start at 8 mJy beam^{-1} and increase by a factor 2.

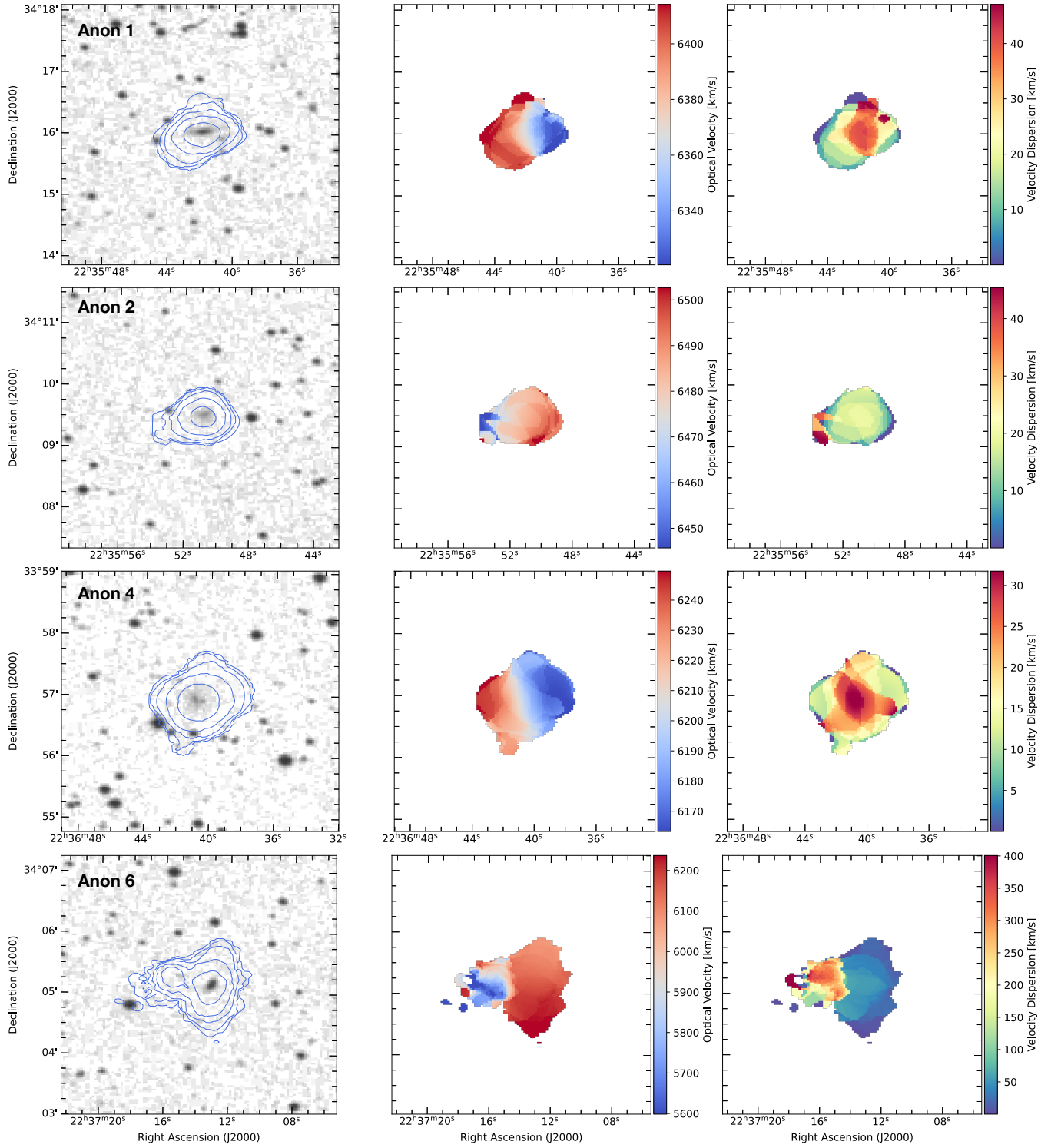


Figure A.4. MeerKAT H I column density distribution contours overlaid on DSS (left), first-order moment of the radial velocity field (middle) and the second-order moment of the velocity dispersion of neighboring galaxies in the field. H I contour levels are plotted at $5.6, 11.1, 22.3, 44.5, 89.1, 178, \dots \times 10^{19}$ atoms cm^{-2} . The beam size is $25'' \times 25''$.

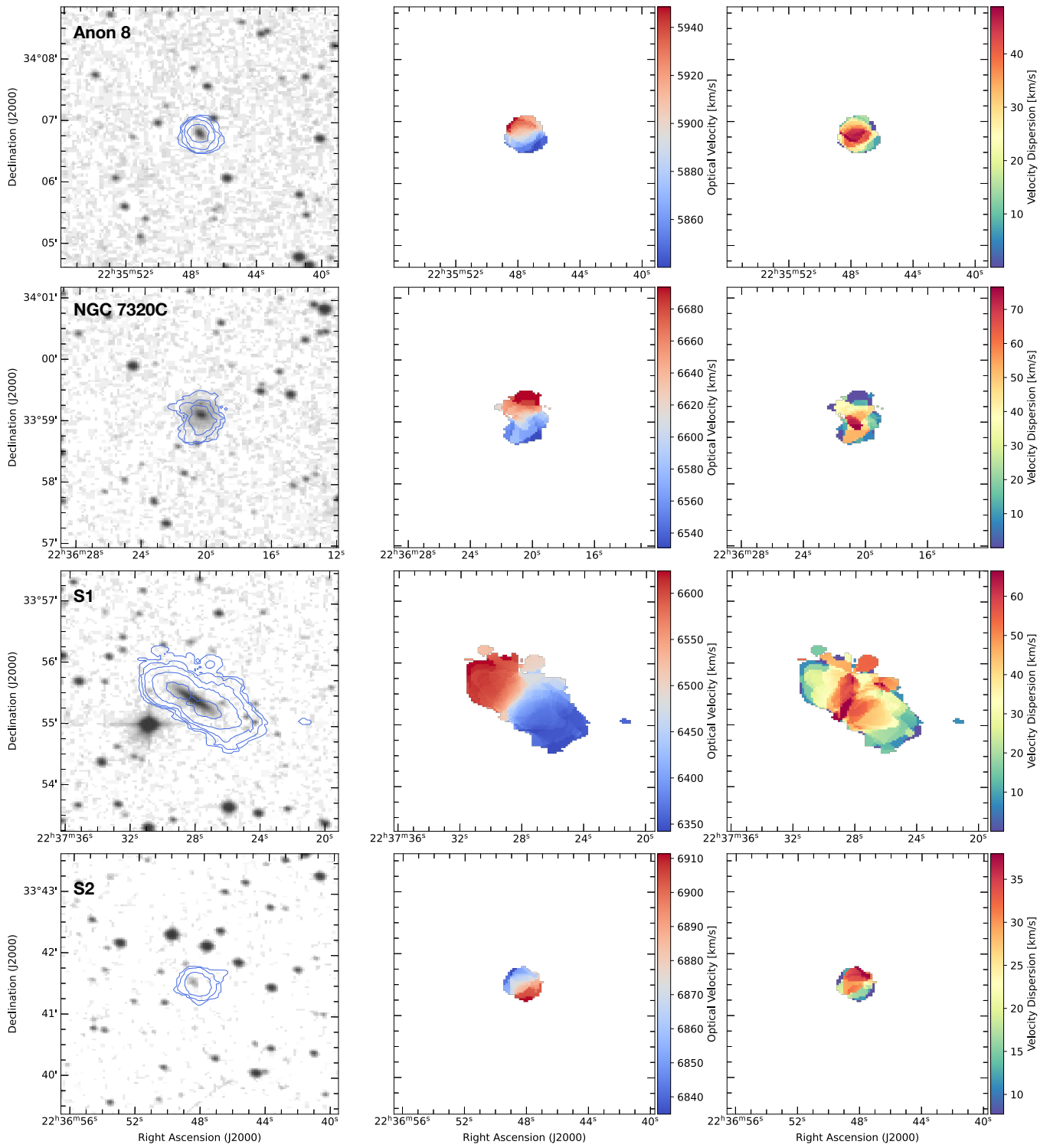


Figure A.5. Continued. The beam size and HI contour levels are the same as in Figure A.4.

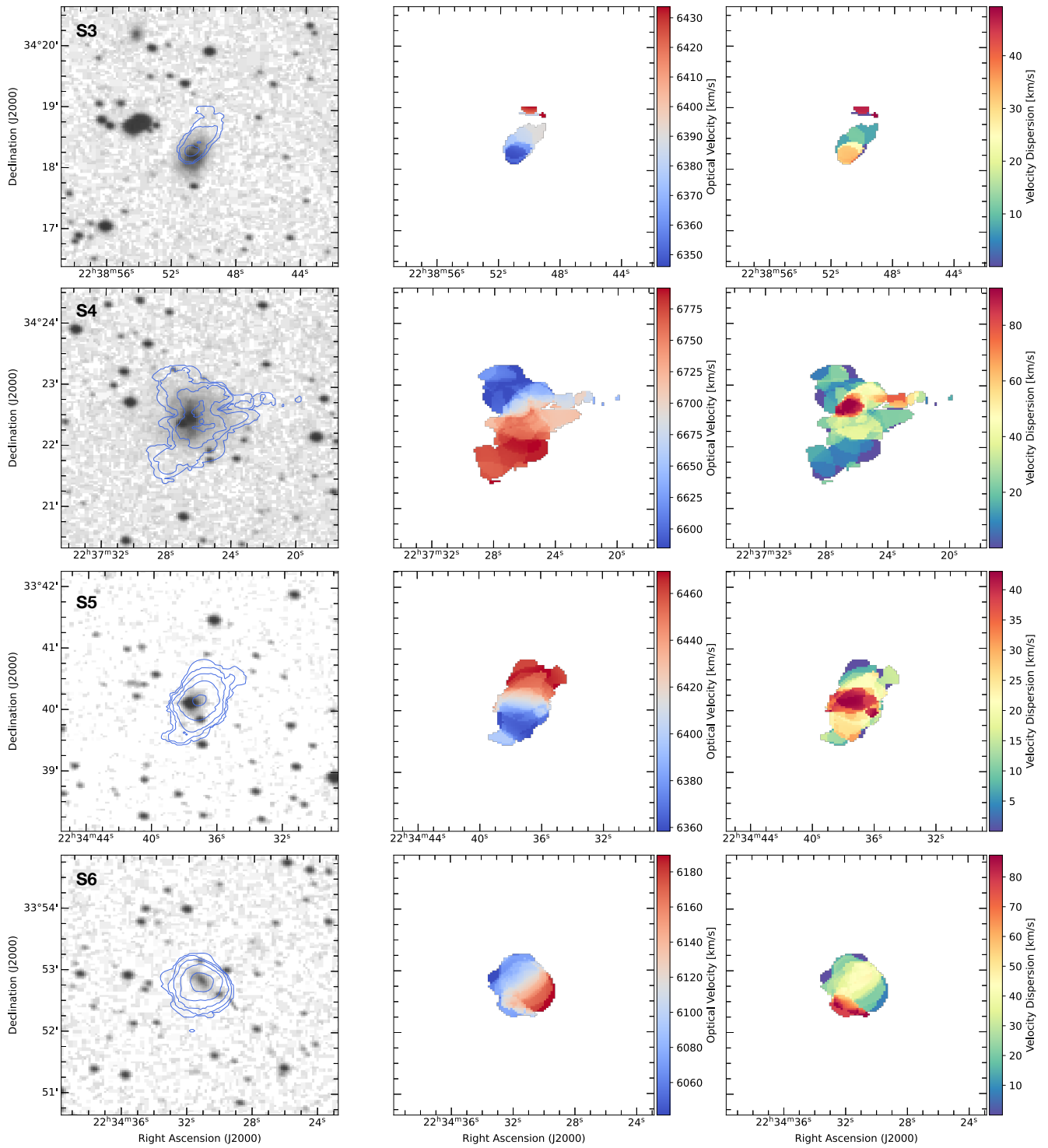


Figure A.6. Continued. The beam size and H I contour levels are the same as in Figure A.4.

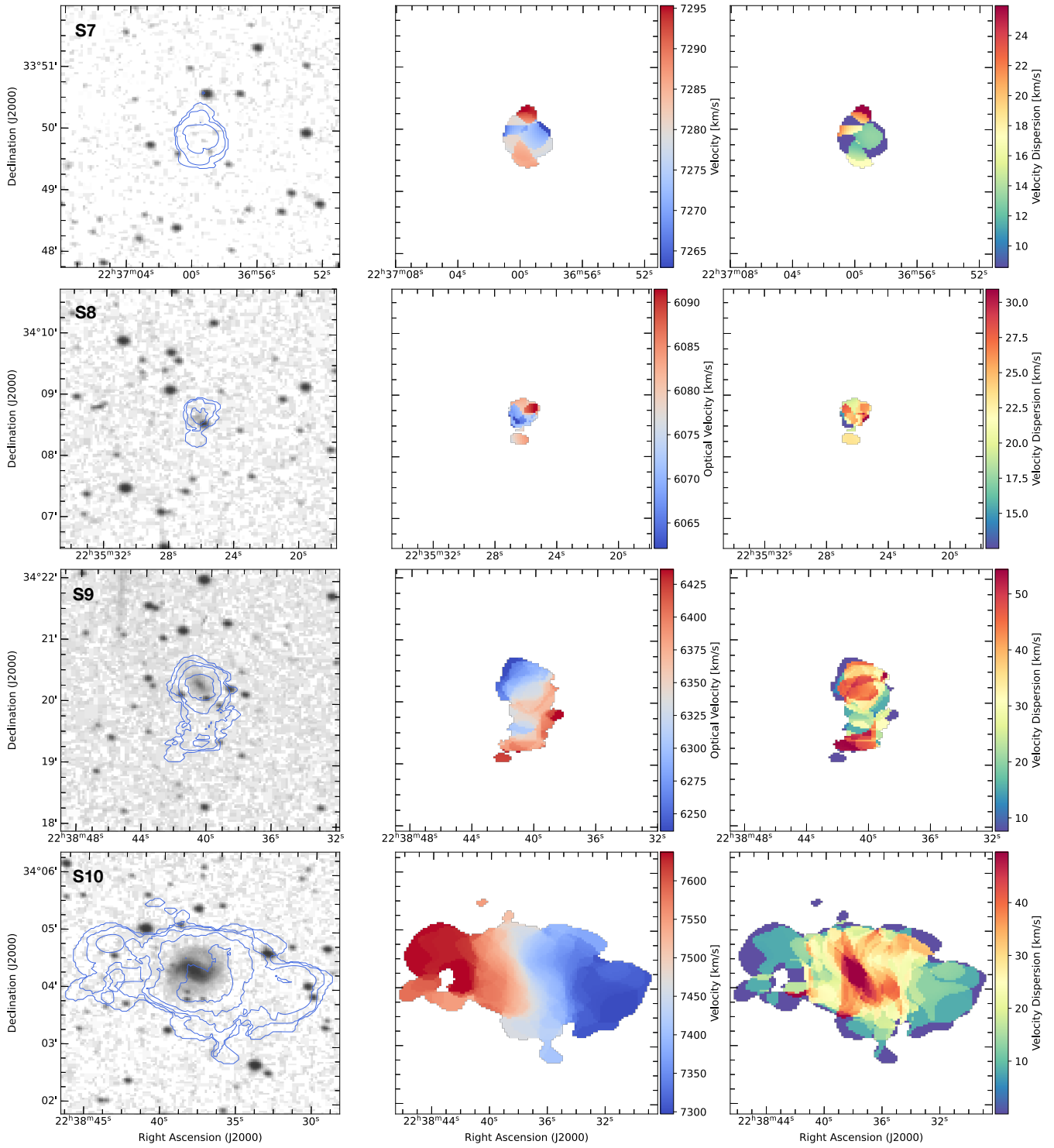


Figure A.7. Continued. The beam size and HI contour levels are the same as in Figure A.4.